Lithos 304–307 (2018) 135–154

Contents lists available at ScienceDirect

Lithos

journal homepage: www.elsevier.com/locate/lithos

Permian charnockites in the Pobeda area: Implications for Tarim mantle plume activity and HT metamorphism in the South Tien Shan range

Chloé Loury [a], Yann Rolland [a,b,*], Pierre Lanari [c], Stéphane Guillot [a], Delphine Bosch [d], Clément Ganino [b], Anthony Jourdon [b], Carole Petit [b], Sylvain Gallet [b], Patrick Monié [d], Nicolas Riel [e]

[a] Université Grenoble Alpes, Univ. Savoie Mont Blanc, CNRS, IRD, IFSTTAR, ISTerre, 38000 Grenoble, France
[b] Université Côte d'Azur, CNRS, OCA, IRD, Géoazur, 250 rue Albert Einstein, Sophia Antipolis, 06560 Valbonne, France
[c] Institute of Geological Sciences, University of Bern, Baltzerstrasse 1 + 3, CH3012 Bern, Switzerland
[d] Géosciences Montpellier, UMR 5243, Université Montpellier & CNRS, Place Eugène Bataillon, 34095 Montpellier, France
[e] Department of Earth Sciences, Durham University, Science Labs, Durham DH1 3LE, United Kingdom

ARTICLE INFO

Article history:
Received 31 May 2017
Accepted 24 January 2018
Available online 8 February 2018

Keywords:
Permian magmatism
Charnockite
South Tien Shan
U/Pb and Ar/Ar
Nd, Sr, Hf, Pb isotopes
Mantle plume
Tarim

ABSTRACT

The Permian history of the Central Asian Orogenic belt is marked by large-scale strike-slip faults that reactivate former Paleozoic structures, delineated by widespread alkaline magmatism. The genetic link between the syn-kinematic granitoids emplaced in the Tien Shan range and magmas emplaced within the Tarim Large Igneous Province, and the interaction between this plume and transcurrent tectonics, are still unsolved issues. We investigated the Pobeda massif, in the eastern Kyrgyz Tien Shan, located at the boundary between the Tien Shan range and the Tarim Craton, which exhibits a high-temperature unit. In this unit, Permian magmatism resulted in the emplacement of alkaline charnockites at mid-crustal levels. The primary mineralogical assemblage is nominally anhydrous and made of ortho- and clino-pyroxenes, fayalite, K-feldspar, plagioclase and quartz. These charnockites are associated with partially-molten paragneisses and marbles. Thermobarometry on these rocks indicates that the charnockites emplaced following the intrusion of a melt at a temperature > 1000 °C and pressure of around 6 kbar, corresponding to depth of ~20 km. The resulting thermal anomaly triggered the partial melting of paragneisses. Bulk geochemistry including Sr, Nd, Pb and Hf isotopes suggests that charnockites fit into the Tarim Large Igneous Province magmatic series, with minor crustal assimilation. U-Pb ages on zircons of charnockites and surrounding paragneisses indicate that charnockites intruded and triggered partial melting of the gneisses at c. 287, 275 and 265 Ma. $^{40}Ar/^{39}Ar$ dating on amphibole gives a similar age as the U-Pb age at 276.2 ± 2.0 Ma. $^{40}Ar/^{39}Ar$ dating on biotite from the Charnockite unit marbles gives ages at ca. 256–265 Ma, which shows that exhumation onset directly follows the HT history, and is tentatively correlated to top-to-the-North thrusting of the Charnockite unit in a transpressive context. Additional $^{40}Ar/^{39}Ar$ dating on syn-kinematic white micas from an adjacent transpressive shear-zone indicates continuation of the strike-slip tectonics at shallow crustal levels, after the exhumation of the Charnockite unit, at 248–257 Ma. These results demonstrate that Tien Shan Permian magmatism is linked to the Tarim mantle plume activity. Lithosphere-scale shear zones in the Tien Shan range, could have been responsible for lateral flow focusing of the Tarim mantle plume up to the boundary with the Tien Shan range and subsequent decompression melting resulting in the Permian magmatism observed in the Pobeda area.

1. Introduction

The Permian history of Central Asia is marked by a phase of intense magmatism, which occurred in different tectonic settings. Mantle plumes led to the emplacement of the large igneous provinces (LIP) of the Tarim in NW China (~280–290 Ma) (e.g. Xu et al., 2014; Yang et al., 2007a), of Emeishan in SW China (~259 Ma) (e.g. Ali et al., 2005 and references therein), and in Siberia (~248 Ma) (e.g. Renne and Basu, 1991). In the Tien Shan and Altai orogens, Permian magmatism is featured by granitic intrusions (e.g. Biske et al., 2013; de Jong et al., 2009; Wang et al., 2009). This phase of intense magmatism affected the Tien Shan belt during early–middle Permian times (290–260 Ma) (Biske et al., 2013; C.L. Zhang et al., 2010; Konopelko et al., 2007, 2009; Wang et al., 2009; Y. Zhang et al., 2010; Yang et al., 2007a). Some authors ascribed the Permian magmatism to a regional-scale strike-slip tectonic regime, as suggested by the spatial extent of plutons, which are elongated along the strike-slip faults (e.g. B. Wang et al., 2014; F. Wang et al., 2014; Konopelko et al., 2007, 2009; Shu et al., 1999; Wang et al., 2009). However, other authors proposed that the

* Corresponding author.
E-mail address: yann.rolland@geoazur.unice.fr (Y. Rolland).

https://doi.org/10.1016/j.lithos.2018.01.025
0024-4937/

Tien Shan Permian magmatism was linked to the Tarim mantle plume activity and thus that the Tarim LIP extents up to the Tien Shan range (e.g. C. L. Zhang et al., 2010; Pirajno, 2010; Xu et al., 2014).

Due to the vast area impacted by the Permian magmatism, highly diversified in terms of geochemistry, age, and tectonic setting, it remains a major issue to understand the post-collisional evolution of the Tien Shan range and its adjacent areas. Especially, the relationships between the Tien Shan and the Tarim magmatism, which are looked either as resulting from a unique or from two distinct processes, is a matter of debate. Due to its difficult accessibility, the Pobeda area, located in the southern part of the South Tien Shan, at the boundary with the Tarim basin (Fig. 1) is still poorly studied. In this area, a high-temperature unit (HT) is exhumed, along a major fault showing evidence of associated magmatism (Loury et al., 2015). Therefore, it is a suitable area to investigate the Permian magmatism in the Tien Shan range and the Tarim Craton and to identify the possible interactions between mantle plume magmatism and strike-slip tectonics. The aim of this study is to provide the first petrological, geochemical and geochronological dataset on this Charnockite unit in order to constrain the origin of the magmatism and the timing of its emplacement. These data coming from the boundary between the Tien Shan range and the Tarim, clarify the relationships between the Tien Shan and the Tarim magmatism and the mantle-plume activity during Permian times.

2. Geological setting

The geology of the Kyrgyz Tien Shan and neighbouring regions is briefly summarized below. For more detailed information regarding the geology and geodynamics of this region, the reader is referred to Loury et al. (2015).

2.1. General framework

2.1.1. Accretion history

The Tien Shan range, located in the southwestern part of the Central Asia Orogenic Belt (CAOB) extends for 2500 km from Uzbekistan to western China. It results from the amalgamation of different blocks during Paleozoic times. In Kyrgyzstan, the Tien Shan range is classically divided into three main units: the North, Middle and South Tien Shan (NTS, MTS and STS respectively, Fig. 1). The NTS itself is an amalgamation of continental fragments, island arcs and ophiolites that were accreted prior to the Middle Ordovician (e.g. Kröner et al., 2013; Mikolaichuk et al., 1997). The Kyrgyz MTS constitutes the southern extremity of the 2000-km long Precambrian Ishim-Middle Tien Shan continent, which extents up to northwestern Kazakhstan (Avdeev and Kovalev, 1989). The MTS basement is overlain by Neoproterozoic to Upper Carboniferous sedimentary series (Tursungaziev and Petrov, 2008). The STS is a Late Paleozoic fold-and-thrust belt resulting from the collision of the MTS to the north with the Tarim Craton to the south in the Late Carboniferous times following the closure of the Turkestan Ocean (Biske, 1995; Hegner et al., 2010; Jourdon et al., 2017a; Loury et al., 2015, 2016). The orientation of the subduction is still a matter of debate: structural evidences along the STS suture, underlined by high-pressure low-temperature units, suggest that the subduction of the Turkestan Ocean was probably south-dipping (e.g. Charvet et al., 2011; Loury et al., 2015) although other authors proposed a north-dipping subduction (e.g. Makarov et al., 2010; Windley et al., 1990). The collision of the Tarim Craton with the Kazakhstan microcontinent is one of the last events of accretion/collision in the Tien Shan range.

2.1.2. Post collisional history

From the Late Carboniferous to Permian times (312–250 Ma), the post-collisional history is marked by a transition toward a strike-slip tectonic regime throughout the CAOB, related to the rotations of different blocks in the Tien Shan with respect to Siberia and Tarim (B. Wang et al., 2007; Laurent-Charvet et al., 2003; Rolland et al., 2013). $^{40}Ar/^{39}Ar$ dating of syn-kinematic white mica along the Talas-Fergana dextral strike-slip fault indicated that this ductile shearing initiated in the late Carboniferous time, around 312–317 Ma and was followed by several episodes of shearing around 290 Ma and 256–250 Ma with brittle reactivation during the Triassic and Jurassic (Konopelko et al., 2013; Rolland et al., 2013). Other radiochronological data, such as U-Pb dating of zircon in syn-kinematic granitoids or $^{40}Ar/^{39}Ar$ dating of syn-

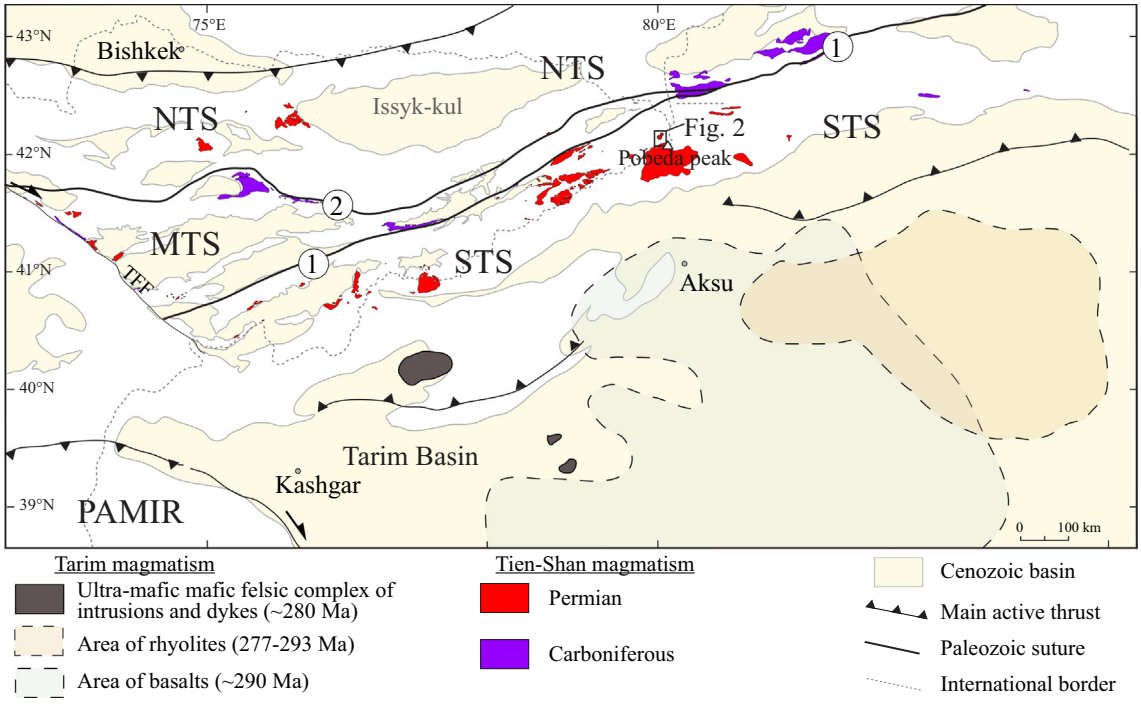

Fig. 1. General tectonic scheme of western Tien Shan and Tarim focusing on Carboniferous and Permian magmatism. Tien Shan magmatism is after Tursungaziev and Petrov (2008) and H. L. Wang et al. (2007) and Tarim magmatism after Xu et al. (2014) and Wei et al. (2014). 1-Atbashi-Nalati Suture; 2-Terksey Suture; TFF: Talas Fergana fault, kSTS: Kyrgyz South Tien Shan.

kinematic white mica, agree for the initiation of strike-slip tectonics, mainly along the Paleozoic sutures zones, ca. 290 Ma ago and further until 245 Ma (e.g. F. Wang et al., 2014; Konopelko et al., 2009; Laurent-Charvet et al., 2003). Coeval with wrench tectonics, widespread intracontinental magmatism affected the Tien Shan range and the northern Tarim Craton. This magmatism is ascribed either directly to the strike-slip tectonics (B. Wang et al., 2014; de Jong et al., 2009; Shu et al., 1999; Wang et al., 2009) or to mantle plume activity unrelated to the local tectonic setting (e.g. Yang et al., 2013 and references therein; Zhang and Zou, 2013; Zhou et al., 2009). In the Tien Shan range, the Late Carboniferous to Permian magmatism is mainly characterized by calc-alkaline to alkaline granitoids (I- and A-types), and by various volcanic or hypo-volcanic rocks such as andesite, rhyolite, trachyte or basalts (e.g. B. Wang et al., 2014; H. L. Wang et al., 2007; Konopelko et al., 2007, 2009; Tursungaziev and Petrov, 2008; Wang et al., 2009). The Tarim magmatism is characterized by a large volume of flood basalts, ultramafic, mafic and felsic dykes complexes and occasional diamandiferous kimberlites (e.g. Tian et al., 2010; Wei and Xu, 2011; Xu et al., 2014; Y. Zhang et al., 2010; Yang et al., 2007a, 2007b).

2.2. The Pobeda area

2.2.1. State of the art

The study area lies in the South Tien Shan, in eastern Kyrgyzstan, close to the northwestern China border. We refer to this area as the Pobeda area, which is close to the Pobeda Peak, the highest summit (7439 m) of the Tien Shan range.

This area exhibits a nappe stack of Paleozoic metamorphic sediments, Devonian to Carboniferous in age (Fig. 2) (Jourdon et al., 2017a; Loury et al., 2015; Mikolaichuk and Buchroithner, 2008). The maximal temperatures recorded by similar metamorphic sedimentary series in the Khan-Tengri massif, northward of the Pobeda are of 570–600 °C (Jourdon et al., 2017a). Deformation analysis of these nappes indicates a first top-to-the-South deformation phase, which is reworked by a second top-to-the-

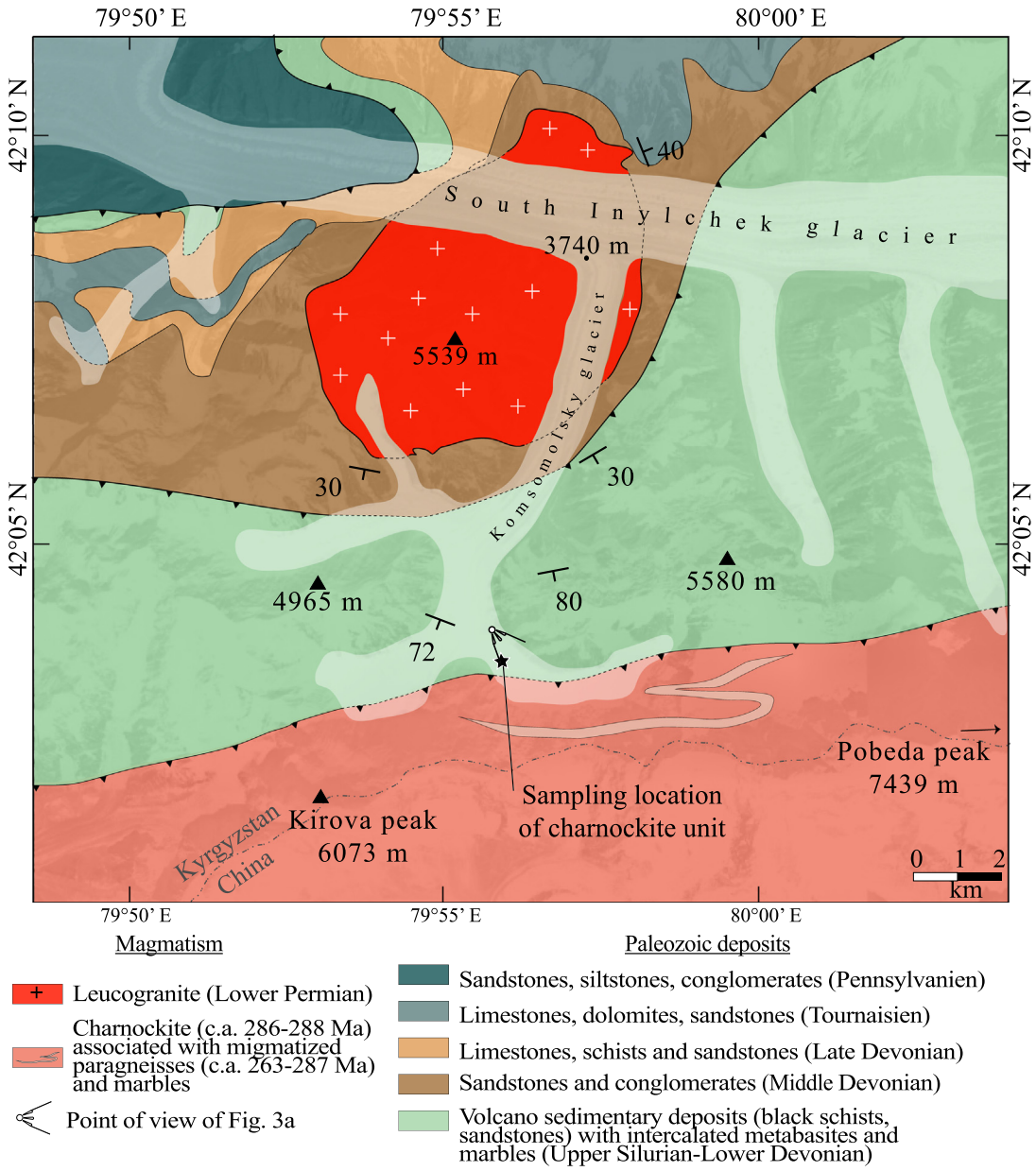

Fig. 2. Geological map of the Pobeda area (modified after Loury et al. (2015) and Mikolaichuk and Buchroithner (2008)). Point of view of Fig. 3a is indicated.

North deformation phase (Jourdon et al., 2017a). In the Pobeda area, this nappe system is intruded by a leucocratic peraluminous granite, mainly made of K-feldspar, quartz and tourmaline (Fig. 2) (Konopelko et al., 2009; Loury et al., 2015). The intrusion age was not directly determined. It is however part of the Inylchek complex of intrusions to the west, which is dated at 289–299 Ma (Konopelko et al., 2009). Southward, the low-metamorphic grade sedimentary series are overthrusted northward by a Charnockite unit along a major fault that is recalled the "Pobeda

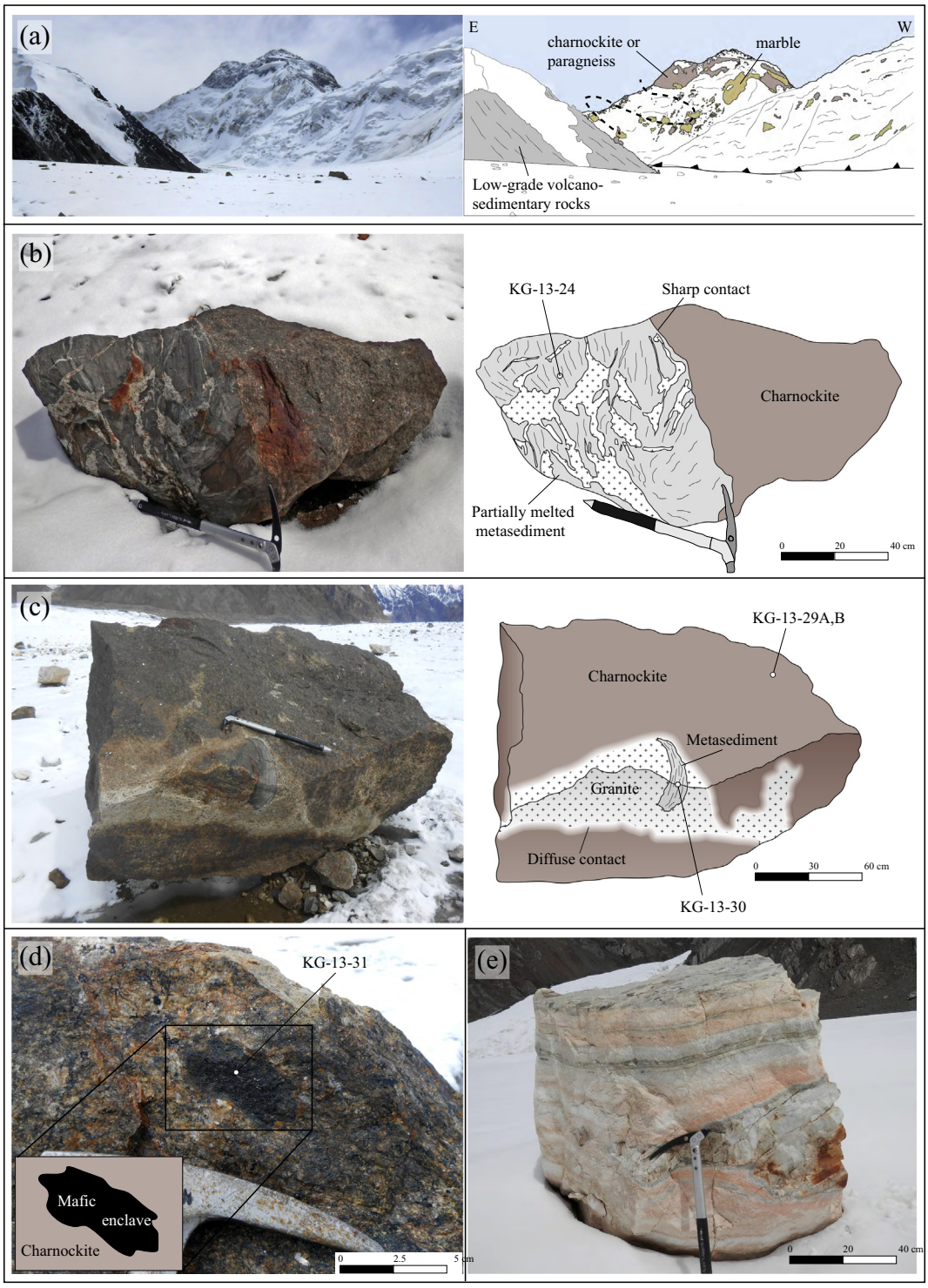

Fig. 3. Field photography of the Pobeda area showing the structure, the different lithologies and samples location. (a) View toward the high-grade unit (left) and interpretation (right). The high-grade unit is overthrusted onto low-grade volcano-sedimentary series. The steepness of the slope and avalanches makes the area inaccessible, however marbles and paragneisses or charnockites can be distinguished on a color basis and marbles show horizontal isoclinal folds. (b) Photography of a meter scale block on the glacier (left) and interpretative sketch (right) showing a sharp contact between a migmatized paragneiss (sample KG-13-24) and a charnockite. (c) Photography of a metric charnockite block (sample KG-13-29A and B) on the glacier (left) and interpretative sketch (right) showing a more diffuse contact than in (b) between a dyke of granite resulting from partial melting of paragneiss and a charnockite. A restite of metasediment is visible in the granite dike (sample KG-13-30). (d) Charnockite block with a mafic enclave (sample KG-13-31). (e) Marble block showing an extended sigmoid layer of quartzite. The mafic enclave does not show any foliation or any preferred orientation, which suggests a magmatic origin. This mafic enclave is the most primitive component, probably representing the mantle-derived melt, which intruded paragneisses at mid-crustal levels.

thrust" (Loury et al., 2015). These HT rocks, composed of two-pyroxene bearing charnockites, migmatized paragneisses and marbles (Fig. 3a) (Loury et al., 2015) are the focus of this study.

2.2.2. Petrography of the Charnockite unit

The Charnockite unit crops out in a remote zone of the Pobeda Massif and constitutes the highest part of the mountain range, partly hidden below steep glacial slopes (Fig. 3a). The steep slopes are washed away by landslides and avalanches, which provide fresh samples of different lithologies providing textural information for their relationships between 4500 and 6500 m elevation. The paragneisses (Fig. 3) contain mainly feldspar, quartz, biotite and pyroxene. They show a typical migmatitic texture with leucosomes and residues (Fig. 3b). The products of partial melting are locally segregated to form dm- to m-scale granitic dykes (Fig. 3c). The second main lithology is composed by clino- and ortho-pyroxene and olivine-bearing charnockites. Contact between paragneisses and charnockites is systematically sharp (Fig. 3b), whereas it is more diffuse between charnockites and leucosomes and granitic dykes (Fig. 3c). Mafic enclaves, of a few centimeters in width, are observed in the charnockites (Fig. 3d). The third lithology of the Charnockite unit is made of epidote-tourmaline bearing marbles (Fig. 3e), which appear to form recumbent isoclinal folds within the metasediments in the landscape (Fig. 3a).

These textural relations suggest that charnockites were intruded in partially melted paragneisses with several lines of evidence of mixing between charnockites and migmatite melts. The intrusive nature of the charnockites indicates an igneous origin. Therefore, we used the term 'charnockite' following Frost and Frost (2008) who defined charnockites as orthopyroxene- or fayalite-bearing quartzo-feldspathic igneous rocks to avoid any confusion with "granulite facies metamorphism".

3. Analytical procedures

3.1. EPMA data acquisition

Mineral compositions of the different studied lithologies were acquired using a JEOL JXA-8200 electron probe micro-analyzer (EPMA) at the Institute of Geological Sciences (University of Bern) and a JEOL JXA-8230 EPMA at the Institut des Sciences de la Terre (Université Grenoble Alpes). All measurements were acquired in wavelength-dispersive mode with the following setup: 15 keV accelerating voltage, 12 nA specimen current for all minerals except olivine which was analyzed at 300 nA. Structural formulae were calculated on an 8 anhydrous oxygen basis for feldspar, 4 for olivine, 6 for pyroxene, 23 for amphibole and 11 for biotite (Tables 1–5). Fe^{3+} content was estimated using the method of Holland and Blundy (1994) for amphibole and charge-balance for pyroxene introducing the ferric end-member acmite.

3.2. Major-trace elements and Sr-Nd-Hf-Pb isotopic analyses

Fresh samples of charnockites, mafic enclave and granite were crushed and powdered in an agate mill. Whole-rock analyses were performed at the CRPG of Nancy (France) following the procedure of Carignan et al. (2001). Major element concentrations were obtained by ICP-OES analyses and trace element concentrations were obtained by ICP-MS analyses (Table 6).

For Sr, Nd, Pb and Hf isotopic analyses, whole rocks were leached for 45 min in 6 N HCl at 90 °C. After leaching, residues were rinsed three times in purified Milli-Q H_2O. Samples were subsequently dissolved during 72 h on a hot plate with a mixture of HF-HNO_3-$HClO_4$ (1:1:0.2) followed by a final digestion step in a Milestone microwave during 45 min. After evaporation to dryness, 1 mL of HNO_3 was added

Table 1
Representative chemical composition (in oxide wt%) of feldspar and corresponding structural formulae calculated on an 8 anhydrous oxygen basis.

	Charnockite		Metasediment				Granite (partial melting of gneisses)	
	KG-13-31		KG-13-30		KG-13-24		KG-13-28	
	K-Feldspar	Plagioclase	K-Feldspar	Plagioclase	K-Feldspar	Plagioclase	K-Feldspar	Plagioclase
Composition (ox. wt%)								
SiO_2	64.73	61.64	64.63	61.12	64.67	58.76	64.82	65.71
TiO_2	0.01	0.02	0.01	0.02	0.01	0.00	0.02	0.00
Al_2O_3	18.55	24.20	18.52	24.80	18.81	26.58	18.65	22.06
FeO	0.16	0.29	0.13	0.14	0.27	0.05	0.13	0.12
MnO	0.01	0.00	0.01	0.00	0.03	0.00	0.02	0.01
MgO	0.00	0.00	0.00	0.00	0.00	0.00	0.00	0.00
CaO	0.00	5.46	0.00	5.91	0.00	7.97	0.00	2.42
Na_2O	0.68	8.70	0.65	8.49	0.82	7.07	0.40	10.38
K_2O	15.75	0.17	15.76	0.15	15.60	0.17	16.12	0.17
Cr_2O_3	0.00	0.02	0.00	0.01	0.00	0.01	0.00	0.00
Sum	99.89	100.49	99.71	100.64	100.20	100.61	100.16	100.88
Structural formuluae (pfu)								
Si	2.99	2.73	2.98	2.70	2.98	2.61	2.99	2.87
Ti	0.00	0.00	0.00	0.00	0.00	0.00	0.00	0.00
Al	1.01	1.26	1.00	1.29	1.02	1.39	1.01	1.13
Fe	0.01	0.01	0.00	0.01	0.01	0.00	0.01	0.00
Mn	0.00	0.00	0.00	0.00	0.00	0.00	0.00	0.00
Mg	0.00	0.00	0.00	0.00	0.00	0.00	0.00	0.00
Ca	0.00	0.26	0.00	0.28	0.00	0.38	0.00	0.11
Na	0.06	0.75	0.06	0.73	0.07	0.61	0.04	0.88
K	0.93	0.01	0.92	0.01	0.92	0.01	0.95	0.01
Cr	0.00	0.00	0.00	0.00	0.00	0.00	0.00	0.00
Sum	4.99	5.02	4.97	5.02	5.00	5.00	4.99	5.01
End-members proportion								
An	0.00	0.25	0.00	0.28	0.00	0.38	0.00	0.11
Ab	0.06	0.74	0.06	0.72	0.07	0.61	0.04	0.88
Or	0.94	0.01	0.94	0.01	0.93	0.01	0.96	0.01

Table 2
Representative chemical composition (in oxide wt%) of olivine and corresponding structural formulae calculated on a 4 anhydrous oxygen basis.

	Charnockite mafic enclave
	KG-13-31
Composition (ox. wt%)	
SiO_2	29.86
TiO_2	0.01
Al_2O_3	0.00
FeO	66.09
MnO	1.70
MgO	1.56
CaO	0.08
Na_2O	0.00
K_2O	0.00
Cr_2O_3	0.01
Sum	99.31
Structural formulae (pfu)	
Si	1.00
Ti	0.00
Al	0.00
Fe	1.86
Mn	0.05
Mg	0.08
Na	0.00
Ca	0.00
K	0.00
Cr	0.00
Sum	2.99
End-members proportion	
XFa	0.94
XFo	0.04
XTeph	0.02

Table 3
Representative chemical composition (in oxide wt%) of pyroxene and corresponding structural formulae calculated on a 6 anhydrous oxygen basis. Fe^{3+} was estimated using charge-balance introducing the ferric acmite end-meer.

	Charnockite				Metasediment	
	KG-13-31 - felsic zone		KG-13-29B - felsic zone	KG-13-31 - mafic enclave	KG-13-30	KG-13-24
Composition (ox. wt%)						
SiO_2	49.14	47.98	*48.61*	53.11	52.77	52.99
TiO_2	0.08	0.10	*0.20*	0.03	0.13	0.12
Al_2O_3	0.55	0.19	*0.96*	0.35	0.75	0.99
FeO	24.40	45.52	*24.71*	9.17	9.23	9.40
MnO	0.54	1.22	*0.00*	0.22	0.22	0.16
MgO	4.31	5.26	*3.46*	12.88	12.95	12.81
CaO	20.15	0.74	*20.31*	24.00	23.61	23.96
Na_2O	0.28	0.04	*0.32*	0.13	0.24	0.16
K_2O	0.02	0.00	*0.02*	0.00	0.00	0.01
Sum	99.48	101.05	98.59	99.90	99.90	100.59
Structural formulae (pfu)						
Si	1.98	2.00	1.98	1.99	1.98	1.98
Ti	0.00	0.00	0.01	0.00	0.00	0.00
Al	0.03	0.01	0.05	0.02	0.03	0.04
Fe^{2+}	0.82	1.58	0.84	0.29	0.28	0.29
Fe^{3+}	0.00	0.00	0.00	0.00	0.01	0.00
Mn	0.02	0.04	0.00	0.01	0.01	0.01
Mg	0.26	0.33	0.21	0.72	0.72	0.71
Ca	0.87	0.03	0.89	0.97	0.95	0.96
Na	0.02	0.00	0.03	0.01	0.02	0.01
K	0.00	0.00	0.00	0.00	0.00	0.00
Sum	4.01	4.00	4.00	4.00	4.01	4.00
End member proportion						
Xen	0.13	0.16	0.11	0.36	0.37	0.36
Xwo	0.44	0.02	0.46	0.49	0.48	0.49
XFs	0.42	0.80	0.43	0.15	0.14	0.15

to the residue and kept at about 90 °C for 36 h and then evaporated to dryness. The Pb chemical separation was done using anion resin and HBr and HCl as eluants. Sr isotopes were separated using Sr Eichrom resin and REE were concentrated from the matrix using cation exchange resin followed by two steps of Nd purification using the HDEHP technique. Sr, Nd, Pb and Hf total procedural blanks were <40 pg, 10 pg, 15 pg and 10 pg, respectively. Sr, Nd, Pb and Hf isotopic compositions were measured using the Neptune Plus Thermo-Fisher Scientific MC-ICP-MS from the Ecole Normale Supérieure de Lyon. Details about analytical parameters, including reproducibility, accuracy and standards, are available in Bosch et al. (2008) and references therein. εNd and εHf were calculated using the CHUR composition of Bouvier et al. (2008).

3.3. U-Pb dating

LA-ICPMS U-Pb dating of zircon was performed on the charnockites and on the granite resulting from the paragneisses partial melting. For charnockites KG-13-29A and KG-13-29B, analyses were done in situ on regular 30 μm thick thin sections. The granites KG-13-27 and KG-13-28 were crushed and sieved to <500 μm. Zircons were separated based on density and magnetic properties before handpicking. Selected grains where then mounted in epoxy and polished down to near equatorial sections. SEM VP-SE imaging was carried out on all zircon grains before LA-ICPMS analyses.

Zircon U-Th-Pb dating and trace-element analyses were performed at the Institute of Geological Sciences (University of Bern) using a GeoLas-Pro 193 nm ArF Excimer laser system (Lambda Physik, Germany) combined with an Elan DRC-e quadrupole mass spectrometer (Perkin Elmer, USA). The LA-ICPMS procedure was similar to those described in Kunz et al. (2017). The laser was operated at a repetition rate of 9 Hz and surface energy density of 2.5 $J \cdot cm^{-2}$. For aerosol transport, a mixture of He (1 $L \cdot min^{-1}$) and H_2 (0.008 $L \cdot min^{-1}$) was used (see Burn et al., 2017 for the detailed analytical conditions). The instrument was tuned before each analytical session to optimize the sensitivity of the heavy masses and the oxide production (ThO^+/Th^+) was always suppressed to <0.5%. The laser spot diameter was set to 24 μm for charnockites and 32 μm for granites. Analyses of unknowns were bracketed by the zircon standard GJ1 (Jackson et al., 2004) for U-Pb calibration and the synthetic SRM612 glass from the National Institute of Standards and Technology (NIST) was used as primary standard reference material to calculate the trace element concentrations. Accuracy and long term reproducibility was monitored using the zircon secondary standard Plešovice (337.13 ± 0.37 Ma; Sláma et al., 2008). The Iolite 2.5 software (Paton et al., 2011) using Petrus and Kamber (2012) VizualAge data reduction scheme and the error propagation method built into Iolite was used to calculate the $^{206}Pb/^{238}U$, $^{207}Pb/^{235}U$, $^{207}Pb/^{206}Pb$ and $^{208}Pb/^{232}Th$ ratios and final ages. Concordia diagrams and age calculations were made with Isoplot 3.0 (Ludwig, 2003). As ages are younger than 1000 Ma, the $^{206}Pb/^{238}U$ ages were preferred. Uncertainties are quoted at 2σ. A detailed table of results is given in Appendix A1. The compilation of U-Pb ages is presented in Table 8.

3.4. $^{40}Ar/^{39}Ar$ dating

In order to constrain the cooling history of the Charnockite unit, $^{40}Ar/^{39}Ar$ dating was performed on the marble sample KG-13-22 and granite sample KG-13-27. Samples were crushed down to a 500–800 μm size fraction and cleaned in an ultrasonic bath. Biotite grains from sample KG-13-22, and amphibole grains from sample KG-13-27 were carefully handpicked under a binocular microscope to select only grains without any trace of alteration or inclusions. Selected grains were packed in aluminum foils and irradiated for 40 h in the Triga Mark II nuclear reactor of Pavia University in Italy together with Fish Canyon sanidine grains as flux monitor (28.03 ± 0.08 Ma,

Table 4
Representative chemical composition (in oxide wt%) of amphibole, corresponding structural formulae calculated on a 23 anhydrous oxygen basis and atome site distribution. Fe^{3+} content was estimated following the method of Holland and Blundy (1994). Amphibole name is given following the classification of Leake (1978).

	Charnockite					Metasediment		Granite (partial melting of gneisses)
	KG-13-31 - felsic zone		KG-13-29B - felsic zone	KG-13-31 - mafic enclave		KG-13-30	KG-13-24	KG-13-28
	Ferro-tschermakitique hornblende	Anthophyllite	Hastingsitic hornblende	Actinolite	Ferroan-pargasitic hornblende	Actinolite	Actinolite	Hastingsitic hornblende
Composition (ox. wt%)								
SiO_2	41.50	50.14	40.57	53.19	42.72	52.55	53.81	40.28
TiO_2	1.13	0.04	0.85	0.19	1.36	0.11	0.17	1.06
Al_2O_3	9.97	0.32	10.16	2.95	13.04	2.93	3.31	9.89
FeO	28.57	40.04	29.43	12.39	13.89	14.44	9.88	32.36
MnO	0.27	0.69	0.00	0.21	0.17	0.18	0.19	1.28
MgO	3.27	5.89	3.05	15.72	11.36	14.70	17.51	0.40
CaO	10.61	0.83	10.80	12.47	12.03	12.27	12.57	10.20
Na_2O	1.46	0.11	1.50	0.54	1.81	0.61	0.40	1.70
K_2O	1.21	0.01	1.82	0.17	1.72	0.32	0.23	1.40
Sum	97.99	98.06	98.18	97.83	98.10	98.11	98.07	98.57
Structural formulae (pfu)								
Si	6.49	7.97	6.40	7.62	6.32	7.57	7.57	6.43
Ti	0.13	0.00	0.10	0.02	0.15	0.01	0.02	0.13
Al	1.84	0.06	1.89	0.50	2.28	0.50	0.55	1.86
Fe^{2+}	3.07	5.32	3.27	1.26	1.61	1.42	0.84	3.59
Fe^{3+}	0.67	0.00	0.62	0.22	0.11	0.32	0.33	0.73
Mn	0.04	0.09	0.00	0.03	0.02	0.02	0.02	0.17
Mg	0.76	1.39	0.72	3.36	2.51	3.16	3.67	0.09
Ca	1.78	0.14	1.83	1.91	1.91	1.89	1.90	1.74
Na	0.44	0.03	0.46	0.15	0.52	0.17	0.11	0.53
K	0.24	0.00	0.37	0.03	0.32	0.06	0.04	0.28
Atome site distribution								
Si(T)	6.49	7.97	6.40	7.62	6.32	7.57	7.57	6.43
(Ca + Na)(B)	2.00	0.16	2.00	2.00	2.00	2.00	2.00	2.00
Na(B)	0.22	0.02	0.17	0.09	0.09	0.11	0.10	0.26
(Na + K)(A)	0.46	0.02	0.65	0.09	0.75	0.12	0.05	0.56
Fe^{2+} / (Fe^{2+} + Mg)	0.20	0.21	0.18	0.73	0.61	0.69	0.81	0.03
Fe^{3+} / (Fe^{3+} + Alvi)	0.67	0.00	0.68	0.66	0.16	0.83	0.73	0.72

Jourdan and Renne, 2007). For this reactor, the following correction factors for argon nuclear interferences were applied after irradiation of pure salts of KF and CaF_2: $(^{36}Ar/^{37}Ar)_{Ca} = 0.000288 \pm 0.000016$; $(^{39}Ar/^{37}Ar)_{Ca} = 0.000727 \pm 0.000041$; $(^{40}Ar/^{39}Ar)_k = 0.00969 \pm 0.00038$; $(^{38}Ar/^{39}Ar)_k = 0.01297 \pm 0.00045$. All samples were analyzed by single-grain infrared CO_2 laser fusion analysis, and isotopic ratios were measured using an ARGUS VI multi-collector mass spectrometer at Geoazur laboratory of Nice University and at Geosciences Montpellier (France). System blanks were measured every three experiments. Mass discrimination for the mass spectrometer was monitored by regularly analyzing air pipette volumes. The ArArCalc © software v2.5.2 was used for data processing. Decay constants are those given by Steiger and Jäger (1977). Uncertainties on apparent and plateau ages are given at the 1σ level including the error on the $^{40}Ar^*/^{39}Ar_k$ ratio of the monitor. The criteria we used for defining a plateau age are: (1) computation on at least 70% of total ^{39}Ar released, (2) at least three successive step-heating fractions, (3) the integrated age of the plateau, calculated by a weighted average of apparent ages of individual fractions constituting the plateau, should be consistent with each apparent age of the plateau within a 2σ uncertainty. Ages referred below as "pseudo-plateau" are those satisfying the statistical conditions of a plateau age with <70% released ^{39}Ar. A detailed table of results is given in Appendix A2. Synthesis of ages is presented in Table 8.

4. Petrography and mineral chemistry

4.1. Charnockites

Two samples of charnockites were analyzed with EPMA: KG-13-29B and KG-13-31. Charnockites are medium to coarse grained with a porphyro-granoblastic texture (Fig. 4a–d). The characteristic mineral assemblage is nominally anhydrous with K-feldspar (~40–45 vol%) + plagioclase (~25–30 vol%) + quartz (~5–10 vol%) + olivine (3–5 vol%) + clinopyroxene (10–15 vol%) + orthopyroxene (~2–3 vol%) + ilmenite (<2 vol%) ± zircon ± apatite. Charnockite was thus classified a quartz-mangerite following the charnockite classification of Streckeisen (1974). Following the IUGS igneous rocks classification (Le Bas and Streckeisen, 1991), it is a fayalite-orthopyroxene–bearing quartz monzonite. However, for clarification, we use the general term charnockite to designate these rocks as proposed by Frost and Frost (2008).

Amphibole occurs as a secondary phase. K-feldspar occurs as porphyroblasts of up to 1–2 mm length and it is generally perthitic. Plagioclase occurs as smaller grains, generally of 0.2 to 0.5 mm size and is oligoclase to andesine in composition with up to 26 mol% anorthite (Fig. 6a, Table 1). Intergrowths of plagioclase and quartz forming myrmekites frequently crystallized around K-feldspar. Olivine, pyroxene and ilmenite are grouped in small granoblastic areas among feldspar and quartz (Fig. 4a–c). Grains are 0.2 to 0.4 mm in size. Olivine is homogeneous and has a fayalite composition (94 mol%) (Table 2). Clinopyroxene is light green and has an augite or hedenbergite composition (Fig. 6b, c, Table 3). It frequently shows orthopyroxene exsolutions (Fig. 4b, d). Orthopyroxene also occurs as distinct grains (Fig. 4c, d) with a ferrosilite composition (80 mol%) (Table 3). Dark green calcic amphibole crystallized around clinopyroxene and has a ferro-tschermakitic to hastingsitic hornblende composition depending on the amount of Na + K (Fig. 7, Table 4). Similarly, orthoamphibole crystallized around orthopyroxene and has an anthophyllite composition (Table 4). Biotite is occasionally associated to secondary amphibole.

The mafic enclaves found in charnockites have a fine-grained texture and are made of amphibole (~45–50 vol%) + biotite (~3–6%) +

Table 5
Representative chemical composition (in oxide wt%) of micas and corresponding structural formulae calculated on a 11 anhydrous oxygen basis.

	Mafic enclave	Metasediment		Granite (partial melting of gneisses)
	KG-13-31	KG-13-30	KG-13-24	KG-13-28
Composition (ox. wt%)				
SiO_2	38.37	40.38	38.64	34.76
TiO_2	2.61	1.88	3.47	3.51
Al_2O_3	14.78	13.19	15.29	15.83
FeO	14.70	13.00	13.83	32.42
MnO	0.04	0.11	0.07	0.22
MgO	15.96	18.08	15.42	1.78
CaO	0.00	0.00	0.06	0.00
Na_2O	0.20	0.04	0.04	0.06
K_2O	8.93	10.18	9.61	9.30
Sum	95.59	96.85	96.42	97.89
Structural formuluae (pfu)				
Si	2.84	2.93	2.83	2.76
Ti	1.29	1.13	1.32	1.48
Al	0.15	0.10	0.19	0.21
Fe	0.91	0.79	0.85	2.15
Mn	0.00	0.01	0.00	0.01
Mg	1.76	1.96	1.68	0.21
Ca	0.00	0.00	0.00	0.00
Na	0.03	0.01	0.01	0.01
K	0.84	0.94	0.90	0.94
XMg	0.66	0.71	0.67	0.09
Sum	7.81	7.87	7.77	7.77
End-members proportion				
XAnn	0.11	0.18	0.08	0.06
XPhl	0.22	0.44	0.16	0.01
XSid	0.18	0.10	0.22	0.81
XEas	0.36	0.24	0.45	0.08
XWhiteMica	0.13	0.05	0.09	0.05

Table 6
Chemical compositions of charnockite, mafic enclave and granite resulting from partial melting of paragneiss.

	Charnockite		Mafic enclave	Granite
	KG-13-29A	KG-13-29B	KG-13-31	KG-13-27
Major elements (ox. wt%)				
SiO_2	62.27	62.81	42.99	74.09
Al_2O_3	15.41	14.71	9.31	12.51
Fe_2O_3	7.51	7.99	13.20	2.96
MnO	0.13	0.13	0.19	0.04
MgO	0.38	0.38	8.28	0.11
CaO	3.08	3.22	17.03	1.56
Na_2O	3.66	3.60	1.26	2.99
K_2O	5.64	5.03	1.06	4.77
TiO_2	0.65	0.72	1.75	0.26
P_2O_5	0.20	0.22	0.78	0.06
PF	0.10	0.00	2.85	0.79
Total	99.02	98.80	98.71	100.15
Trace elements (ppm)				
Cs	1.19	1.04	0.14	1.72
Rb	147.30	137.30	31.68	152.20
Ba	918.60	678.10	510.70	616.10
Th	2.19	1.99	8.20	7.84
U	1.07	1.29	2.15	1.39
Nb	40.59	49.36	28.20	22.03
Ta	2.17	2.68	1.88	1.48
La	41.01	39.79	51.90	53.44
Ce	83.19	85.81	121.30	99.99
Pb	25.76	24.27	4.40	29.29
Pr	10.22	10.97	15.39	10.84
Sr	164.10	141.20	106.80	125.60
Nd	42.41	46.42	61.79	39.57
Zr	627.00	663.00	338.80	329.00
Hf	14.92	15.87	8.29	7.79
Sm	9.17	10.28	13.79	6.95
Eu	2.76	2.44	1.97	1.41
Gd	7.84	8.81	11.65	5.56
Tb	1.18	1.31	1.85	0.77
Dy	6.94	7.53	10.94	4.32
Y	34.59	38.39	55.60	21.40
Ho	1.39	1.52	2.20	0.83
Er	3.60	3.88	5.62	2.14
Tm	0.52	0.56	0.80	0.29
Yb	3.56	3.76	5.16	1.89
Lu	0.57	0.61	0.76	0.30

plagioclase (~15–20%) + clinopyroxene (25–30%) + titanite ± ilmenite ± calcite ± apatite (Fig. 4e, f). Plagioclase occurs as small grains, <0.1 mm in size. Two types of calcic amphiboles are found (Fig. 4f). Amphibole 1 is a dark green anhedral amphibole, which replaced clinopyroxene and has an actinolite composition (Fig. 7, Table 4). Amphibole 2 is more abundant and occurs as light green to brownish subhedral grains, 0.1 to 0.4 mm in size. It is more alkaline than amphibole 1 and has a ferroan pargasitic hornblende composition. Clinopyroxene is retrogressed and associated with amphibole 1. This association forms pseudomorphs of the primary clinopyroxene grains, of 0.1–0.3 mm size. The latter has a diopside composition (Fig. 6b, Table 3). Biotite is interstitial and is 0.3–0.7 mm in length. The Mg/Mg + Fe^{2+} ratio (XMg) of biotite is 0.66 (Table 5).

4.2. Paragneisses

Two samples of paragneisses were analysed using EPMA: KG-13-24 and KG-13-30 (see Fig. 2 for sampling location). Sample KG-13-24 has a very fine-grained hornfelsic texture (Fig. 5c) and sample KG-13-30 has a fine-grained grano-lepidoblastic texture (Fig. 5a, b), characteristic of granulite facies metamorphism (Turner, 1981). Both are made of K-feldspar + plagioclase + quartz + clinopyroxene + amphibole + biotite + titanite + calcite. KG-13-24 contains also some pyrite grains. The grain size ranges from 0.05–0.1 mm in sample KG-13-24 and 0.1–0.3 mm in sample KG-13-30. Plagioclase has an oligoclase to andesine composition with up to 38 mol% of anorthite in KG-13-24 and 32% in KG-13-30 (Fig. 6a, Table 1). Clinopyroxene has a diopside composition (Fig. 6b, Table 3). In sample KG-13-24, clinopyroxene is strongly retrogressed and replaced by calcic amphibole whereas in KG-13-30, only few grains show a small amphibole corona (Fig. 5a–c). In both samples, amphibole has an actinolite composition (Fig. 7, Table 4). Biotite is magnesian in both samples (XMg = 0.67–0.71) and is more aluminous in KG-13-24, with an eastonite composition, than in KG-13-30, which shows a phlogopite composition (Table 5).

The granite resulting from paragneisses partial melting is either undeformed (sample KG-13-28), or slightly foliated (sample KG-13-27). It is a syeno-granite according to the QAP diagram. Undeformed granite shows a fine to medium grained porphyroblastic texture and contains K-feldpar + plagioclase + quartz + amphibole + biotite + ilmenite ± zircon ± allanite. K-feldspar occurs as porphyroblasts of 0.1 to 1 cm in size with a perthitic texture (Fig. 5d, top-right corner). It is almost pure orthoclase (96 mol%) (Fig. 6a, Table 1). Plagioclase occurs as 0.3 to 0.5 mm grains, and as exsolutions in K-feldspar porphyroblasts. It has an oligoclase composition, with 11% of anorthite (Fig. 6a, Table 1). Amphibole is dark green and grains are 0.1 to 1 mm in size. It has a composition of hastingsite hornblende (Fig. 7, Table 4). Biotite occurs as grains of 0.2 to 0.6 mm length or is associated with quartz in myrmekites, which is a typical magmatic texture (e.g. Touret and Huizenga, 2012)(Fig. 5d). These symplectites generally occur at the contact with K-feldspar. Biotite is ferrous (XMg = 0.09) with a siderophyllite composition.

4.3. Marbles

The marbles have a fined-grained hornfels texture. Sample KG-13-22 contains calcite + epidote + muscovite + biotite + tourmaline +

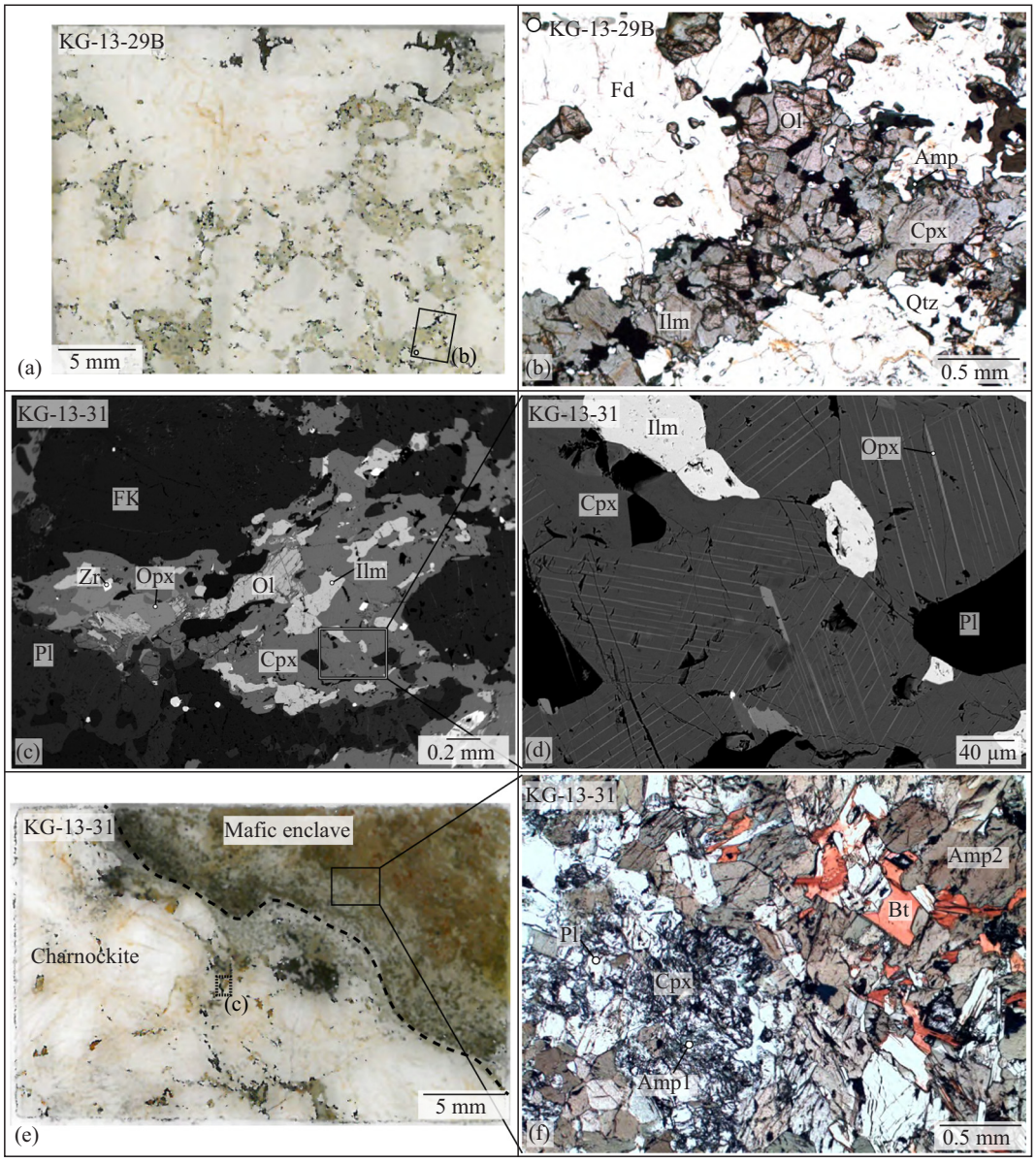

Fig. 4. Photomicrographs of charnockite (samples KG-13-29A and B). (a) A pyroxene + olivine melanosome is surrounded by a leucocratic domain of feldspar + quartz (plane polarized light). (b) Pyroxene and olivine aggregate with clinopyroxene showing orthopyroxene exsolutions (crossed polarized light). (c) Back-scattering-electron (BSE) image showing olivine, clinopyroxene and orthopyroxene. The area of image (d) is shown. (d) BSE image of clinopyroxene showing orthopyroxene exsolutions. (e) Mafic enclave (sample KG-13-31) photomicrographs showing clinopyroxene retrogressed and replaced by amphibole 1 (plane polarized light). (f) BSE image of the mafic enclave (sample KG-13-31). Mineral abbreviations are the following: Amp: amphibole; Bt: biotite; Cpx: clinopyroxene; Ilm: ilmenite; Fd: feldspar; FK: alkaline feldspar; Ol: olivine; Pl: plagioclase; Qtz: quartz; Opx: orthopyroxene; Sph: sphene (or titanite); Zr: zircon.

titanite + plagioclase ± quartz (Fig. 5e, f). Calcite grains are 0.5 to 3 mm in size and are uncolored to light gray. Epidote grains are variable in size, from 0.1 to 3 mm wide.

5. Geochemical composition

Major and trace element contents and Sr, Nd, Pb and Hf isotopic compositions are reported in Tables 6 and 7.

5.1. Major and trace elements

Charnockites (samples KG-13-29A and B) have a SiO_2-rich (62–63 wt%) alkaline chemical composition with $Na_2O + K_2O$ of 8.6 and 9.3 wt% (Fig. 8a). They are potassic, with K_2O = 5–5.6 wt%, and ferroan with a $FeO_T / (FeO_T + MgO)$ ratio of 0.95 which explains the presence of both K-feldspar and Fe-rich phases such as pyroxene or olivine. They are rather poor in TiO_2 (0.65–0.72 wt%). Finally, they are weakly peraluminous with an aluminum saturation index (ASI) of 1.05. Extended trace element diagrams show that charnockites are globally enriched in Large Ion Lithophile Elements (LILEs), Rare Earth Elements (REEs) and High Field Strength Elements (HFSEs) with respect to primitive mantle (Fig. 8c). Trace element repartition shows an enrichment in LILEs and Light Rare Earth Elements (LREEs) with respect to Heavy Rare Earth Elements (HREEs) with a $(La/Yb)_N$ ratio of 7.6 and 8.3, respectively (Fig. 8b). Zr and Hf show a positive anomaly with a $(Zr/Nd)_N$ ratio of 1.73–1.79. Pb also shows a strong positive anomaly [$(Pb/Ce)_N$ = 2.71–2.97] whereas Th and Sr yield negative anomalies [$(Th/U)_N$ = 0.38–0.51 and $(Sr/Nd)_N$ = 0.20–0.25]. Charnockites have overall similar contents as Oceanic Island Basalts (OIBs) for light and medium REEs, while being slightly enriched in HREEs with respect to OIBs (Fig. 8b). The LILEs have

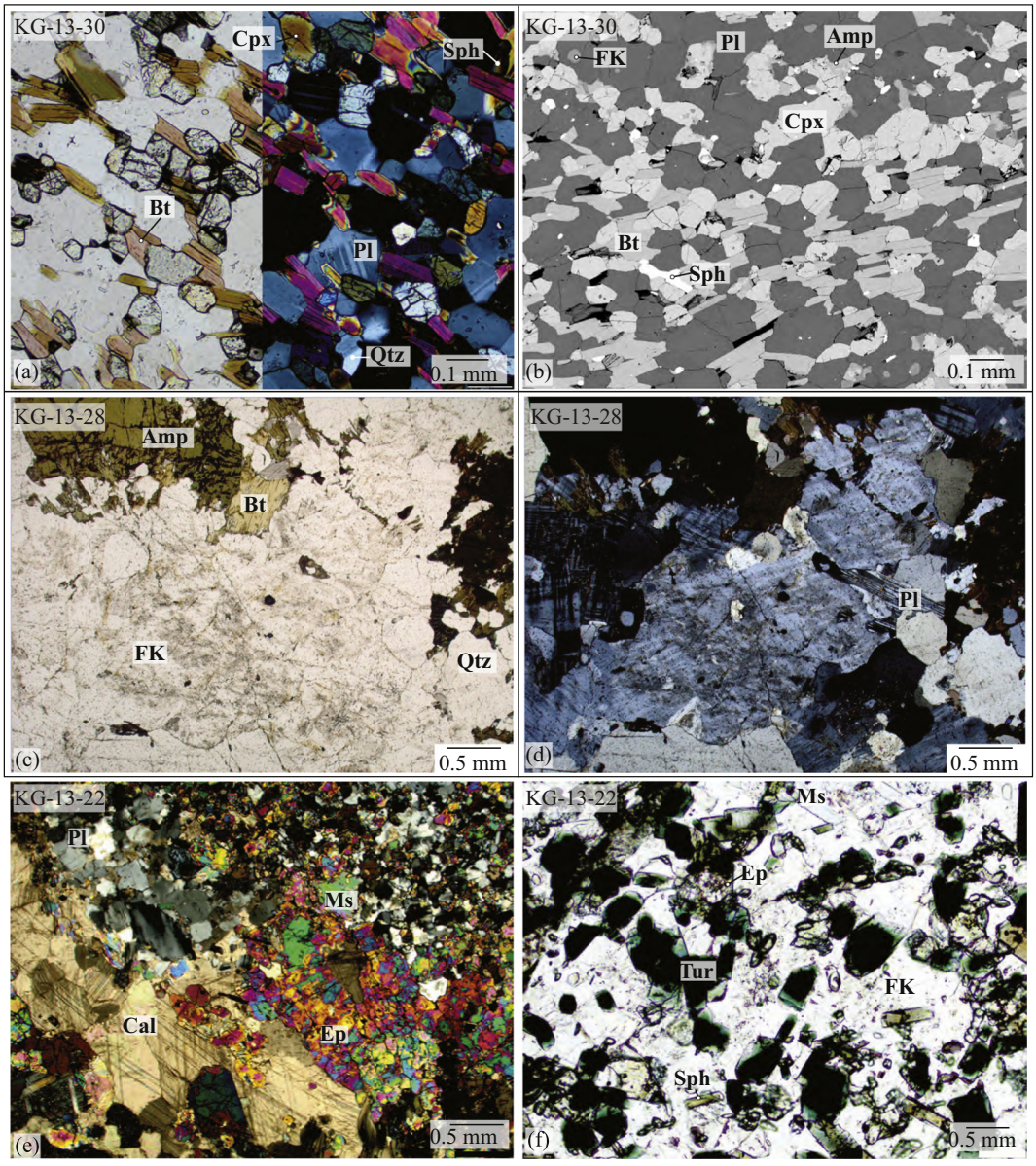

Fig. 5. Photomicrographs of paragneiss, granite and marbles. (a) Paragneiss KG-13-30 showing a grano-lepidoblastic texture, typical of granulite facies metamorphism (plane polarized (left) and crossed polarized (right) lights). (b) BSE image of sample KG-13-30. (c) BSE image of paragneiss KG-13-24 showing a hornfelsic texture. (d) BSE image of a granite resulting from partial melting of paragneiss (sample KG-13-28) showing a perthitic K-feldspar porphyroblast and a quartz-biotite myrmeckite. (e) Sample KG-13-22 of marble showing a fine-grained hornfelsic texture (crossed polarized light). (f) Area of the KG-13-22 sample containing tourmaline (plane polarized light). Mineral abbreviations: see Fig. 5 caption and Cal: calcite, Ep: epidote; Ms: muscovite; Tur: tourmaline.

a variable behavior, the lightest LILEs (Cs, Rb and Ba) and Pb being higher and Th and Sr being lower in charnockites than in OIBs.

The mafic enclave in charnockite sample KG-13-31 has a different composition in terms of major elements. It is SiO_2 poor (43 wt%) and is also alkaline, with $Na_2O + K_2O = 2.33$ wt% (Fig. 8a). The enclave is more magnesian than the charnockite with a $FeO_T/(FeO_T + MgO)$ ratio of 0.61 and has a higher TiO_2 concentration (1.75 wt%). The enclave is metaluminous with an aluminum saturation index of 0.52 and $Na + K < Al$ (Frost et al., 2001). This could explain the crystallization of calcic phases such as diopside or calcic amphibole (amphibole 2). In terms of trace elements, as compared to the charnockites, the mafic enclave has similar pattern but higher REE contents and a marked negative Eu anomaly (Fig. 8b). It is globally enriched in LILEs and REEs with respect to primitive mantle (Fig. 8c). LREEs and LILEs are enriched with respect to HREEs with a $(La/Yb)_N$ ratio of 7.22. HFSEs show negative anomalies in Nb and Ta contents with $(Ta/La)_N$ and $(Nb/La)_N$ ratios of 0.61 and 0.52, respectively, and $(Zr/Nd)_N$ ratio of 0.66. Pb, Sr and Eu show negative anomalies with a $(Pb/Ce)_N$ ratio of 0.35, a $(Sr/Nd)_N$ ratio of 0.11, and a $(Eu/Sm)_N$ ratio of 0.38.

5.2. Sr, Nd, Pb and Hf isotopes

The isotopic composition of analyzed samples yields information on the geochemical signature of the source of magmatic rocks (Table 7). The initial isotopic ratios have been recalculated at 290 Ma, in agreement with the obtained U-Pb ages (Section 7).

The $^{143}Nd/^{144}Nd_i$ of the two charnockites are homogeneous, of 0.51199 and 0.51200 (εNd_i ratios of −5.25 and −5.40, respectively), while the corresponding $^{87}Sr/^{86}Sr_i$ is of 0.70947 (εSr_i of KG-13-29B of 75.42; Fig. 9a). The initial $^{206}Pb/^{204}Pb_i$ ratios, $^{207}Pb/^{204}Pb_i$ and $^{208}Pb/^{204}Pb_i$ of KG-13-29B are of 18.14, 15.66 (Fig. 9b) and 38.48, respectively. KG-13-29A charnockite shows a $^{176}Hf/^{177}Hf_i$ of 0.28266

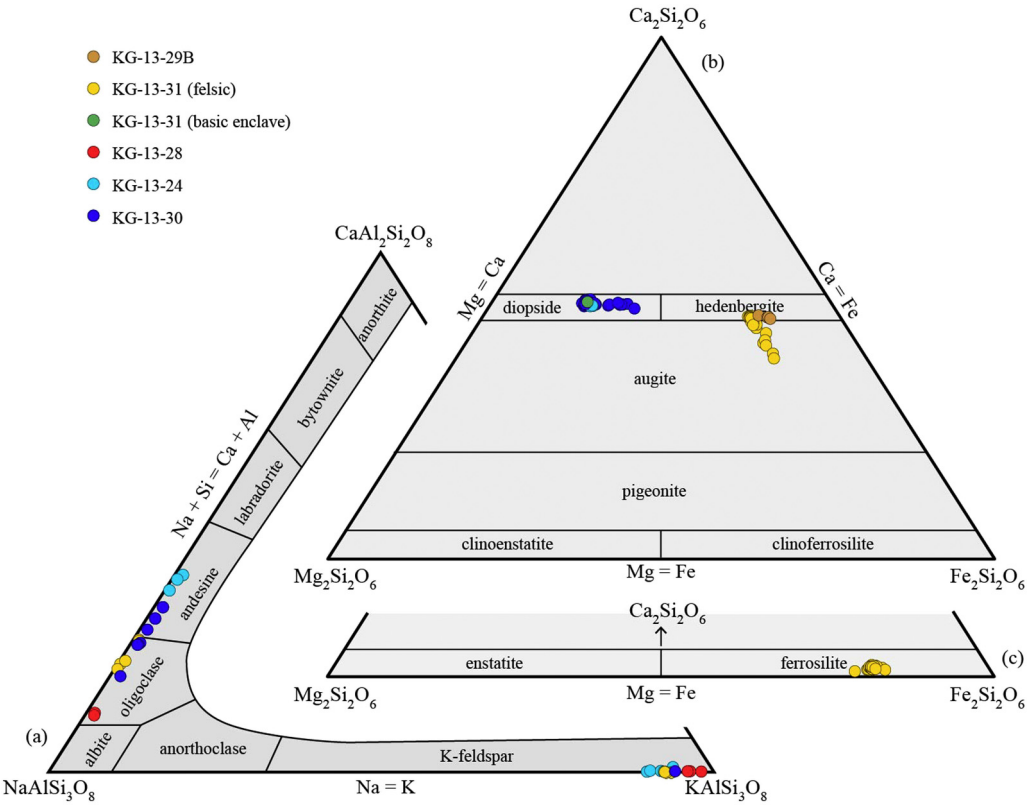

Fig. 6. Mineral composition from EMPA analyses. (a) Feldspar, (b) clinopyroxene, (c) orthopyroxene. The nomenclature of Morimoto (1988) is used for pyroxene.

(corresponding to a εHf_i value of 2.59), in good agreement with values measured for Tarim Permian basalts (Li et al., 2012) (Fig. 9c).

The mafic enclave in charnockite (KG-13-31) bears a εNd_i ratio of 3.84 and εSr_i ratio of 49.27, indicating a clear mantle-derived origin (Fig. 9a). Compared to the OIB field, it shows a comparable εNd_i value but a higher εSr_i value suggesting hydrothermal alteration (e.g. White, 2013). Such a process can potentially affect the budget for mobile elements as Pb, U, etc., which may affect the *in situ* decay correction for Pb isotopic ratios of this sample. Nevertheless, it is noteworthy that the uncorrected $^{206}Pb/^{204}Pb$, $^{207}Pb/^{204}Pb$ and $^{208}Pb/^{204}Pb$ ratios (i.e. 17.73, 15.56 and 38.79, respectively) are similar to the Tarim flood basalts values (Fig. 9b). The εHf_i value is 11.41, comparable to typical OIB values and similar to Tarim basalts (Fig. 9c).

The granite (sample KG-13-27) resulting from paragneiss partial melting, despite slightly lower εHf_i ratio of 10.20, shows higher $^{206}Pb/^{204}Pb_i$, $^{207}Pb/^{204}Pb_i$ and $^{208}Pb/^{204}Pb_i$ ratios, of 19.62, 15.75 and 40.21, respectively, which is in agreement with a crustal origin (Fig. 9b). The slightly lower εHf_i is interpreted as resulting from some local compositional variability, which is not representative of the bulk crustal signature involved in the formation of charnockites.

6. P-T conditions of migmatization and charnockite emplacement

In order to determine the pressure and temperature conditions of charnockite emplacement, forward thermodynamic modeling was used to model phase relationships. An isochemical P-T equilibrium phase diagram was calculated with Perple_X (version 6.7.1, Connolly, 2009) using the internally consistent thermodynamic data set of Holland and Powell (1998) and subsequent updates (hp02ver). The chemical system considered was NKCFMASTi (Na_2O, K_2O, CaO, FeO, MgO, Al_2O_3, SiO_2 and TiO_2). As the only hydrous phases observed in the charnockites are secondary, the chemical system was considered as anhydrous to model the peak assemblage. MnO was excluded as it has a very low content in all measured phases as in the bulk rock composition. The solid solution models used were those of Holland and Powell (1996) for ortho- and clino-pyroxene (Opx(HP) and Cpx(HP)), Holland and Powell (1998) for olivine (O(HP)) and garnet (Gt(HP)), White et al. (2001) for melt (melt(HP)) and Fuhrman and Lindsley (1988) for feldspar (feldspar). Cordierite solution model was assumed to be ideal (hCrd).

The phase diagram in Fig. 10 indicates that melt is stable for the bulk rock composition at temperatures higher than 960 °C at 1 kbar and >1050 °C at 12 kbar. The mineral assemblage observed in charnockites (clinopyroxene – orthopyroxene – olivine – K-feldspar – plagioclase – quartz – ilmenite) is modeled at temperatures lower than 960 °C and pressures below 9 kbar. Mineral modes and compositions are fairly well modeled at P-T conditions of 850 ± 50 °C and 5.5 ± 0.5 kbar except for clinopyroxene which is slightly underestimated (~10–15 vol% observed vs. ~5 vol% modeled).

The pressure conditions of secondary amphibole crystallization in the charnockites were determined using the barometer of Schmidt (1992) based on the Al content in hornblende. This calibration was developed for a granitic assemblage containing the buffering phases hornblende, biotite, K-feldspar, plagioclase and quartz; all of which are present in the Pobeda charnockites. The amphiboles of the charnockites have an Al content of 1.82 to 2.05 pfu, indicating pressure conditions between 5.6 and 6.7 kbar (Fig. 10).

P-T conditions of the KG-13-28 granite resulting from paragneiss partial melting was estimated using the calibration of Holland and Blundy (1994) based on amphibole-plagioclase-quartz equilibrium, at a pressure determined with the barometer of Schmidt (1992), both of which are expected to be reliable for this kind of rock. The homogeneous composition of amphibole together with the absence of diffusion rim at amphibole-plagioclase grain boundary suggests that chemical equilibrium was achieved and maintained between the growing amphibole and plagioclase. Calculations were done for all the amphibole analyses with the mean composition of plagioclase of this sample (Ab_{88}-An_{11}). The amphibole-plagioclase assemblage formed at pressures

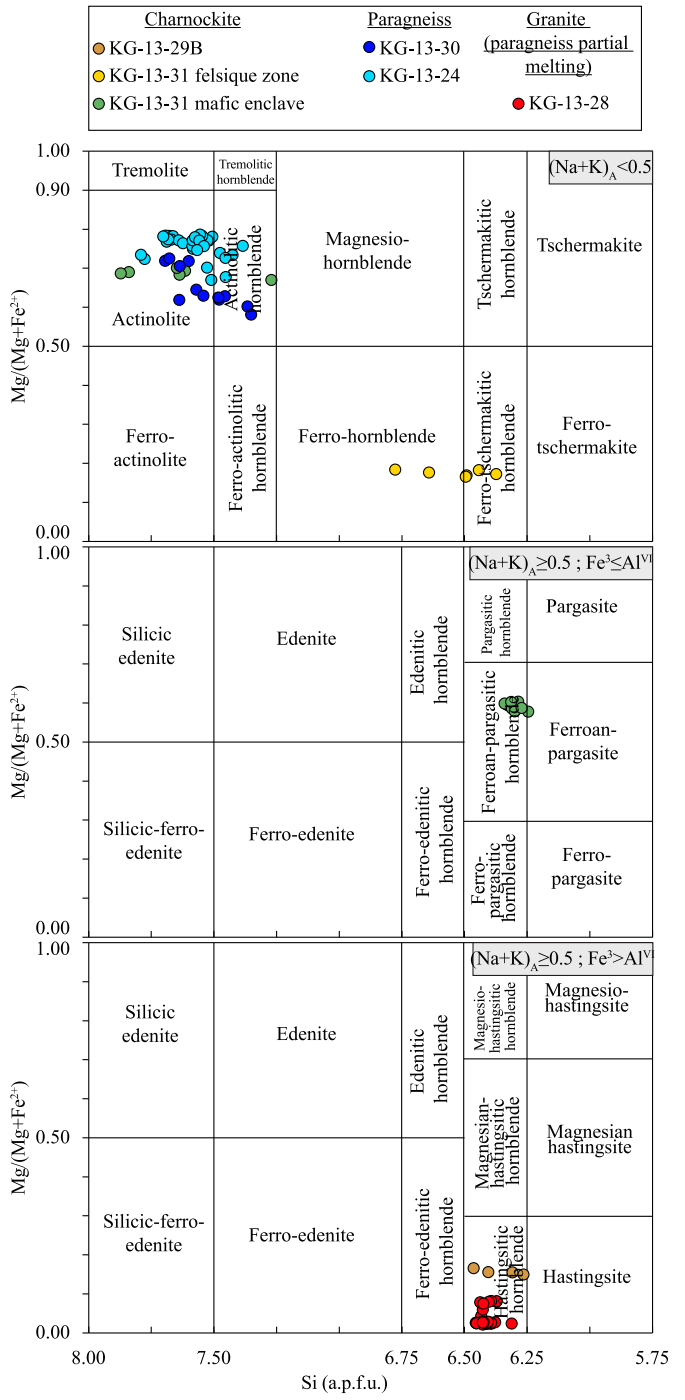

Fig. 7. Calcic-amphibole composition ($(Ca + Na)_B \geq 1.34$; $Na_B < 0.67$ and $Ti < 0.50$) following the classification of Leake (1978).

between 5.7 and 6.6 kbar and temperatures ranging between 550 and 650 °C.

7. U-Pb dating

7.1. Charnockites

Zircon grains from charnockites are euhedral to subhedral and some grains show oscillatory zoning in VP-SE and BSE images (Fig. 11a, b). High Th/U ratios, between 0.35 and 1, with a mean value of 0.59, are consistent with a magmatic origin (Rubatto, 2002). Zircon grains from sample KG-13-29A yield a concordant age of 286.2 ± 3.1 Ma (MSWD = 0.7, n = 14) and a consistent weighted mean age of 285.8 ± 3.2 Ma (MSWD = 0.82) (Fig. 11a). Sample KG-13-29B yields similar results with a concordant age of 289.2 ± 2.5 Ma (MSWD = 2.5, n = 18) and a weighted mean age of 288.1 ± 2.5 Ma (Fig. 11b).

Table 7
Sr, Nd, Pd and Hf isotopic analyses. Initial isotopic ratios have been calculated at 290 Ma according to the results of U-Pb ages (see Section 7).

	Charnockites		Granite	
	Felsic zone		Mafic enclave	
Sample	KG-13-29A	KG-13-29B	KG-13-31	KG-13-27
Measured ratios				
$^{143}Nd/^{144}Nd$	0.512244 ± 1	0.512242 ± 1	0.512717 ± 2	–
$^{147}Sm/^{144}Nd$	0.130707	0.133871	0.134925	–
$^{87}Sr/^{86}Sr$	–	0.721094 ± 2	0.711171 ± 8	–
$^{87}Rb/^{86}Sr$	–	2.817019	0.858513	–
$^{208}Pb/^{204}Pb$	–	38.5518 ± 1	38.7860 ± 3	40.4738 ± 1
$^{207}Pb/^{204}Pb$	–	15.6689 ± 4	15.5589 ± 8	15.7562 ± 4
$^{206}Pb/^{204}Pb$	–	18.2953 ± 4	17.7346 ± 5	19.7635 ± 5
$^{176}Hf/^{177}Hf$	0.282687 ± 8	0.283003 ± 5	0.282977 ± 5	0.282902 ± 7
$^{176}Lu/^{177}Hf$	0.005359	0.005409	0.012869	0.005322
Age corrected ratios (290 Ma)				
$^{143}Nd/^{144}Nd_i$	0.51200	0.51199	0.51246	–
εNd_i	−5.25	−5.40	3.84	–
$^{87}Sr/^{86}Sr_i$	–	0.70947	0.70763	–
εSr_i	–	75.42	49.27	–
$^{208}Pb/^{204}Pb_i$	–	38.475	37.041	40.210
$^{207}Pb/^{204}Pb_i$	–	15.661	15.485	15.749
$^{206}Pb/^{204}Pb_i$	–	18.142	16.334	19.621
$^{176}Hf/^{177}Hf_i$	0.28266	–	0.28291	0.28287
εHf_i	2.59	–	11.41	10.20

7.2. Migmatized paragneisses

Zircon grains from the granite resulting from partial melting of paragneisses (samples KG13-27 and KG13-28, Fig. 11c–e) are euhedral and show an oscillatory zoning varying from one grain to another. They have relatively high Th/U ratios comprised between 0.15 and 0.72, with a mean value of 0.41, also consistent with a magmatic origin (Rubatto, 2002). The plot of relative probability of ages of sample KG-13-27 (inset in Fig. 11c) suggests two groups of ages. The first group yields a concordant age of 287.2 ± 0.9 Ma (MSWD = 1.8, n = 28) and a consistent weighted mean age of 287.0 ± 0.9 Ma (MSWD = 0.65). The second group is younger and yields a concordant age of 275.0 ± 1.8 Ma (MSWD = 1.5, n = 7) and a weighted mean age of 274.6 ± 1.9 Ma (MSWD = 0.5). These two groups of ages represent different zircon grains and no zonation in age was observed within a single grain. The sample KG-13-28 yields a concordant age of 265.6 ± 2.1 Ma (MSWD = 2.8, n = 8) and a weighted mean age of 265.0 ± 2.1 Ma (MSWD = 0.78).

8. $^{40}Ar/^{39}Ar$ dating

8.1. Marble

Five duplicates of biotite grains of the marble sample KG-13-22 were analyzed (Fig. 12). Grain 1 shows a steep staircase shape in the first stages, corresponding to low-temperature stages. Then the apparent age continues increasing gently towards HT steps. A plateau age cannot be calculated from this grain, however a 'pseudo-plateau' is estimated at 260.6 ± 2.5 Ma (MSWD = 2.14), corresponding to 39.1% of total ^{39}Ar, released in 4 steps. Grain 2 shows a slight concave downward shape, with a peak at 254 Ma, interpreted as a minimum age, and a total fusion age at 244.3 ± 1.18 Ma (31 steps, 626 f. of ^{39}Ar released in total). Grain 4 also shows a steep staircase shape in the lowest temperature part of the spectrum. Then a plateau is defined with an age of 256.1 ± 1.7 Ma (MSWD = 1.11) corresponding to 81% of ^{39}Ar released in 17 steps. Grain 5 shows a concave downward shape, as for Grain 2. However,

Table 8
Synthesis of samples location, dating results and ages interpretation.

Sample	Description	Locality	Coordinates		U-Pb age (Ma)	Interpretation	$^{40}Ar/^{39}Ar$ age (Ma)	Interpretation
KG-13-29A	Charnockite	Pobeda area	N42°03′ 54″	E79°55′ 28″	286.2 ± 3.1	Charnockite crystallization	–	–
KG-13-29B			N42°03′ 54″	E79°55′ 28″	289.2 ± 2.5	after mantellic melt intrusion	–	–
KG-13-27	Granite resulting from partial melting of paragneiss	Pobeda area	N42°03′ 54″	E79°55′ 28″	287.2 ± 0.9275.0 ± 1.8	Granite crystallization after partial melting	276.23 ± 1.95 plateau (amp)	Isobaric cooling
KG-13-28			N42°03′ 54″	E79°55′ 28″	265.6 ± 2.1		–	–
KG-13-22	Marble	Pobeda area	N42°03′ 70″	E79°56′ 05″	–	–	256–263 Ma (5 spectra, bt)	Minimum age for cooling linked to exhumation of HT unit

for this grain a 'pseudo-plateau' age is obtained at 263.0 ± 2.4 Ma (MSWD = 1.75), corresponding to 35.6% of total ^{39}Ar released in 5 steps. Finally, the grain Mp shows a continuous staircase shape. The higher temperature steps yield an age of 265.3 ± 3.2 Ma (MSWD = 4.82) corresponding to 30% of total ^{39}Ar released in 6 steps, which is interpreted as a minimum age for this sample.

8.2. Granite resulting from paragneiss partial melting

Results are presented on Fig. 12. The first steps, corresponding to the low temperature part of the spectrum show great error bars due to a very low amount of released gas. Then a plateau is obtained at 276.2 ± 2.0 Ma (MSWD = 2.04) corresponding to 84% of ^{39}Ar released in 4 steps.

9. Discussion

9.1. P-T-t conditions of charnockite emplacement and migmatization

The isochemical phase diagrams suggest that the charnockites were crystallized at a pressure of 5 to 6 kbar, deriving from a HT melt, hotter than 1000 °C (Fig. 10). Al-in hornblende barometry indicates a pressure of 5.6 to 6.7 kbar for secondary amphibole crystallization during cooling of charnockites (Fig. 10). Moreover, semi-empirical thermobarometry on plagioclase and hornblende gives temperatures between 550 and 650 °C and pressures between 5.7 and 6.6 kbar for the crystallization of granite resulting from partial melting of paragneisses. The textural relationships between migmatites and granites point toward a partial melting of paragneisses and subsequent granite crystallization at the same structural level, without any large-scale melt extraction (Fig. 3b). This suggests that the partial melting in paragneisses occurred at similar pressure conditions of ~ 6 kbar as for the crystallization of secondary amphibole in charnockites.

U-Pb dating of zircon from charnockites yields ages of 286.2 ± 3.1 Ma and 289.2 ± 2.5 Ma with Th/U ratios indicating of a magmatic origin. The oldest age obtained on granite zircon resulting from partial melting is 287.2 ± 0.9 Ma. These ages, which are similar within uncertainty, are consistent with paragneisses partial melting triggered by the intrusion of the charnockitic melt.

Considering the thermobarometry results, they indicate that (1) partial melting and granite crystallization occurred at a pressure of ca. 6 kbar and that (2) the beginning of charnockites cooling took place at the same pressure conditions. Moreover, geochronology results indicate that the partial melting of paragneisses was triggered by the intrusion of charnockite melts, it is suggested that the charnockites emplaced at

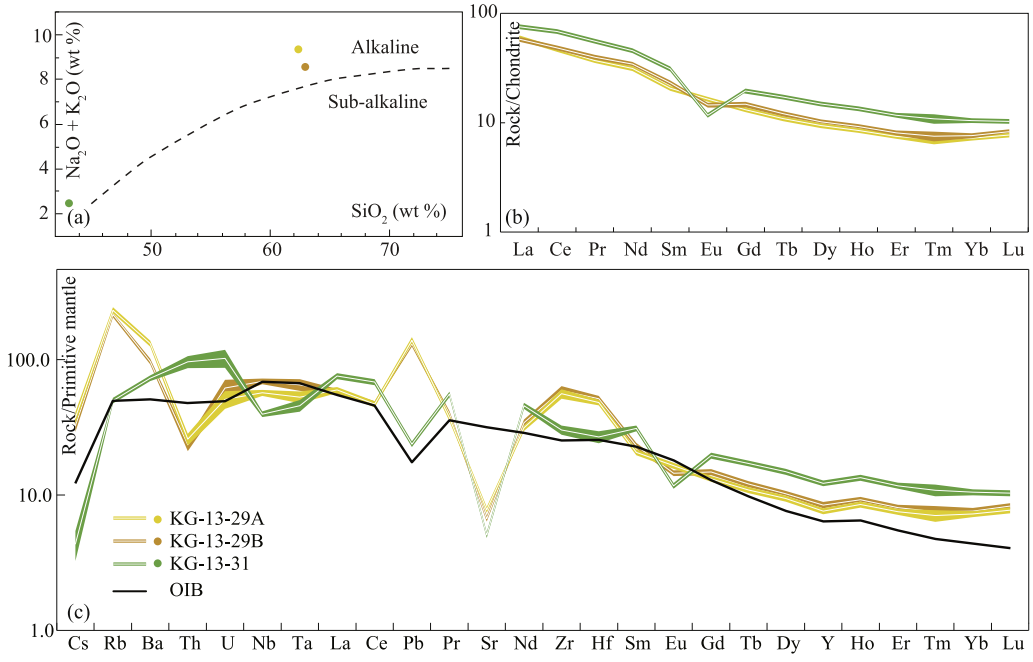

Fig. 8. Major and trace elements geochemistry of charnockite (KG-13-29A and B) and mafic enclave (KG-13-31). (a) SiO_2 vs. alkaline oxides diagram. The alkaline/sub-alkaline line is from Irvine and Baragar (1971). (b) Chondrite normalized rare earth elements (REE) diagram. (c) Primitive mantle normalized spider diagram. Thickness of lines represents the analytical uncertainties. An oceanic island basalt (OIB) composition is shown for comparison. Chondrite and primitive mantle data used for normalization and OIB reference are after Sun and McDonough (1989).

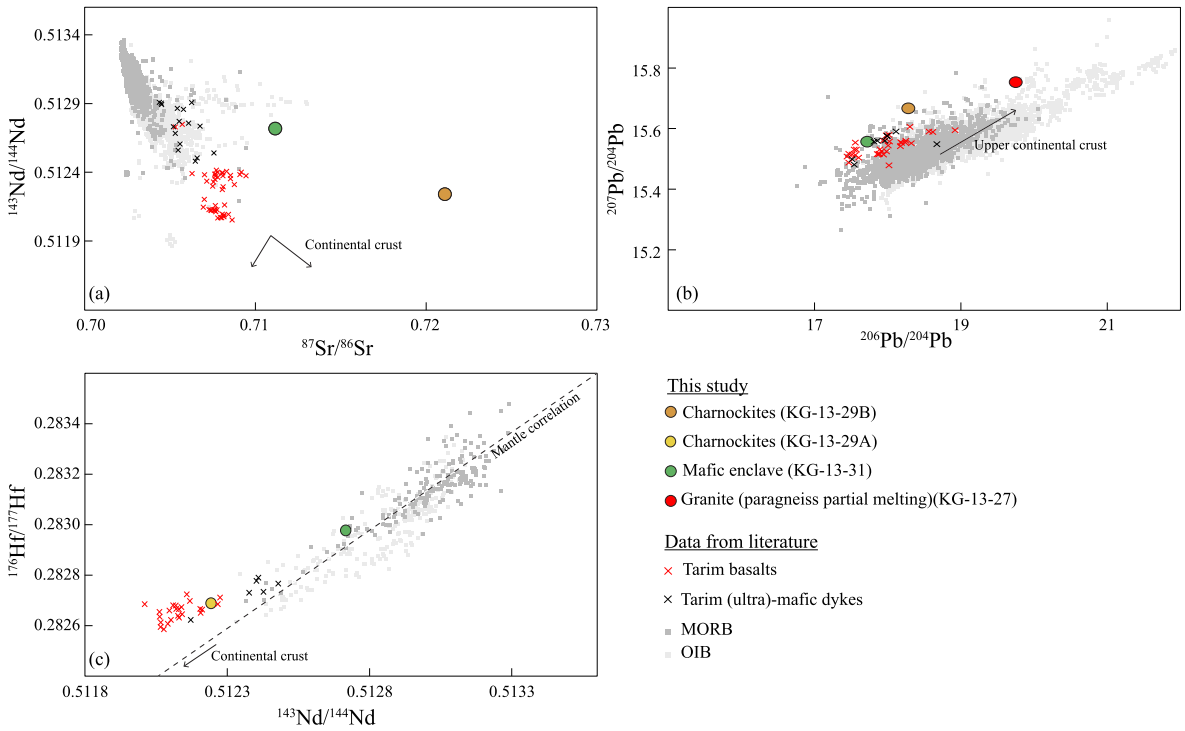

Fig. 9. (a) $^{143}Nd/^{144}Nd$ vs. $^{87}Sr/^{86}Sr$, (b) $^{207}Pb/^{204}Pb$ vs. $^{206}Pb/^{204}Pb$ and (c) $^{177}Hf/^{178}Hf$ vs. $^{143}Nd/^{144}Nd$ diagrams for rocks of the Charnockite unit of the Pobeda area. Fields of Tarim basalts and Tarim dykes are represented for comparison. Data for Tarim basalts are after Li et al. (2012); Wei et al. (2014); Yu et al. (2011); Zhang et al. (2012); Y. Zhang et al. (2010); Zhou et al. (2009) and Tian et al. (2010). For Tarim dykes, data are after Li et al. (2012); Wei et al. (2014); Zhou et al. (2009). The MORB and OIB fields, and the trend towards crustal values are from the GEOROC database [http://georoc.mpch-mainz.gwdg.de/georoc/].

pressures of ca. 6 kbar at around 286–289 Ma. These results also suggest that charnockites were reequilibrated at sub-solidus conditions from a magma emplaced at mid- crustal conditions (corresponding to depth of 19–22 km considering a lithostatic gradient of 0.3 kbar·km^{-1}) when it intruded the metapelitic gneisses and triggered their migmatization.

Three groups of U-Pb ages were obtained on the granites resulting from partial melting of the paragneisses (~287, 275 and 265 Ma, Fig. 11c–e). 287 and 275 Ma old zircons were found in the same sample (KG-13-27). However, only one grain shows a significant difference in age between the core (290.4 ± 4.4 Ma) and the rim (280.7 ± 4.5 Ma). The analyzed grains show typical features of magmatic zircons (high Th/U ratios, oscillatory zoning). $^{40}Ar/^{39}Ar$ dating of amphibole permits dating the cooling or recrystallization of igneous rocks at 500–550 °C (e.g. Harrison, 1982). One amphibole grain from the same sample yields a $^{40}Ar/^{39}Ar$ plateau age of 276.2 ± 2.0 Ma. This age is the same within errors as the 275 Ma age obtained on zircon. It is thus suggested that partial melting of paragneisses and crystallization of granite occurred in a short time range, undistinguishable from the age uncertainty, at 276–275 Ma. It has been shown that mantle-derived melts intruded in continental crust can result in partial melting of continental crust followed by a very fast crystallization (≪1 Ma, Huppert and Sparks, 1988). Therefore, we suggest that the three groups of ages reflect different partial melting episodes, potentially induced by different magmatic intrusions, rather than a continuous process.

9.2. Biotite $^{40}Ar/^{39}Ar$ ages and their geological significance

$^{40}Ar/^{39}Ar$ dating on biotite grains from a marble sample brings information on the cooling history of the Charnockite unit, as the marbles are associated with the paragneisses (Fig. 1a). Only Grain 4 yields a plateau age of 256.1 ± 1.7 Ma. All the grains show disturbed ^{39}Ar releasing pattern with staircased shapes (at least in the low-temperatures steps) or concave downward shapes. These features are typical of grains that have experienced radiogenic argon loss (e.g. Berger, 1975). The obtained $^{40}Ar/^{39}Ar$ biotite age of 256.1 ± 1.7 Ma is thus interpreted as a minimum age for biotite cooling. This cooling age for biotite could either reflect (i) isobaric cooling after the end of magmatism and partial melting, or (ii) the onset of the Charnockite unit exhumation. The closure temperature for argon in biotite is of about 300–350 °C (e.g. Grove and Harrison, 1996). This range of temperature is largely lower than the temperature required for partial melting of paragneisses (~650 °C at 6 kbar; Thompson, 1982), which occurred at least until 265 Ma. An isobaric cooling until from 650 to 300–350 °C would require a minimal cooling rate of 300 °C/Ma, which is too far from rates expected at such a depth (e.g. Chapman and Pollack, 1977). Consequently, the cooling age for biotite, of 256–265 Ma, is rather interpreted as the age of Charnockite unit exhumation. This interpretation is compatible with previous tectonic studies in the Tien Shan area, indicating that the range was affected by a transpressive tectonic regime from 290 to 245 Ma, with a significant reverse component on some major faults (e.g. de Jong et al., 2009; Laurent-Charvet et al., 2003). The Late Permian 256.1 ± 1.7 Ma $^{40}Ar/^{39}Ar$ biotite age is interpreted as resulting from top-to-the-north thrusting occurred along the Pobeda Thrust. It follows that a major part of its motion and its crustal-scale structure were already acquired in the Late Paleozoic, and that limited reactivation occurred along that fault during the Late Cenozoic shortening phase, which is in agreement with numerical modelling and thermochronology (Jourdon et al., 2018, accepted).

9.3. Geochemistry of magmatic rocks of the Pobeda area and comparison with the Tarim mantle plume

Geochronological results suggest that the heat flux induced by this intrusion triggered the paragneiss partial melting (see Section 9.1). Geochemical data on the charnockites and associated mafic enclaves bring new information about the origin of these rocks. Charnockites are SiO_2

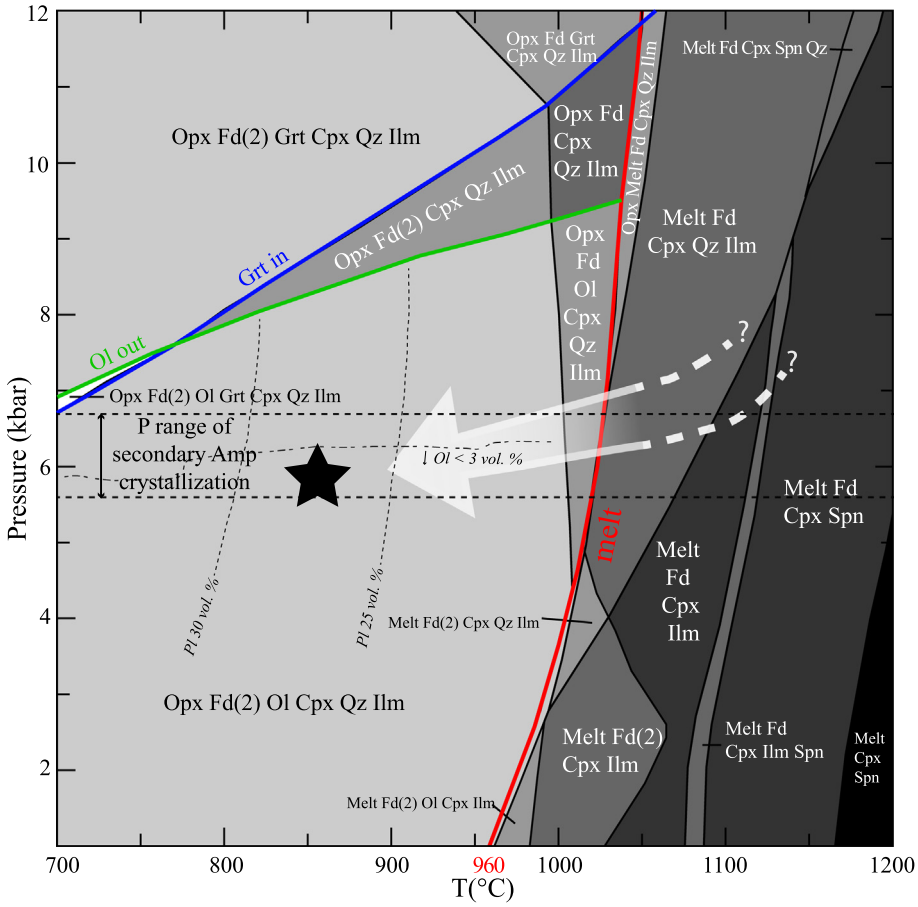

Fig. 10. Isochemical phase diagram computed for the charnockite bulk rock composition (sample KG-13-29A) and inferred P-T path. The red line indicates beginning of partial melting (melt-in reaction). Blue and green lines are for garnet-in and olivine-out reactions, respectively. Dashed lines are isopleths for plagioclase and olivine modes. The star indicates the field corresponding to observed assemblage. Pressure range of secondary amphibole crystallization is shown by black dashed lines. Inferred P-T path is represented by white arrow. Color of the fields indicate the variance (white for variance = 2 and black for variance = 7). Mineral modes are modeled within errors at 5–6 kbar and 800–900 °C, which constrains a smaller P-T field. Only clinopyroxene is underestimated (~10–15 vol% observed vs. ~5 vol% modeled), which is probably due to the presence of a small amount of Fe^{3+}. The corresponding phase composition is also well reproduced (olivine: fayalite 94%, clinopyroxene: hedenbergite, orthopyroxene: ferrosilite 85–87%). The modeled Fe-Ti oxide is ilmenite. Its mode is 0.75 vol%, which is consistent with observations (<2 vol%) and very low oxygen fugacity conditions. Mineral abbreviations: Opx – Orthopyroxene, Cpx – Clinopyroxene, Grt – Garnet, Ol – Olivine, Qz – Quartz, Fd – Feldspar (Fd(2) for the coexistence of two feldspar), Ilm – Ilmenite, Spn – Titanite. (For interpretation of the references to colour in this figure legend, the reader is referred to the web version of this article.)

rich (62–63 wt%) and alkaline in composition (Fig. 3a). They are FeO rich, with a Fe / (Fe + Mg) ratio of 0.95 and HFSEs show positive anomalies (Fig. 3c).

The mafic enclaves potentially represent the most mafic igneous component, which intruded paragneisses at mid-crustal levels. The mantle-derived melt was then mixed with the leucosomes of migmatites (as featured by field relationships) resulting in charnockites formation as suggested by major-trace and isotopic compositions. Analyzed mafic enclave has an alkaline basaltic composition (Fig. 8a) and a Fe/(Fe + Mg) ratio of 0.61. It bears a negative anomaly in HFSEs (Nb, Ta, Zr and Hf) suggesting an influence of subduction-derived fluids in the generation of the mafic magma (e.g. Pearce, 1996). However charnockites are not calc-alkaline, as expected in a subduction setting, and structural and geochronological data from all over the Tien Shan range agree for the end of subduction tectonics by the Late Carboniferous time (e.g. Charvet et al., 2011; Hegner et al., 2010; Konopelko et al., 2007; Li et al., 2011; Wang et al., 2009). Consequently, the subduction components of the mafic magma could be inherited from a metasomatized subcontinental lithosphere mantle and would be compatible with a post-collisional setting. In this case, the inherited subduction component of the mafic enclaves could be an argument for the Carboniferous southward subduction of Middle Tien Shan under the Tarim Craton (e.g. Charvet et al., 2011; Jourdon et al., 2017b; Loury et al., 2015).

The magmatic rocks of the Pobeda area can be related to the Early Permian magmatism occurring over the whole Tien Shan – Tarim region (e.g. de Jong et al., 2009; Gao et al., 2009, 2011). In terms of major elements composition, the charnockites from the Pobeda area tend to be more alkaline than the south Tien Shan granitoids (Fig. 13a). However, the composition of Permian magmatic rocks from the Tarim and the charnockites display a similar alkaline trend (Fig. 13a; e.g., Tian et al., 2010). In terms of REEs composition, they are also very similar to the Tarim basalts (Fig. 13b). In terms of mineralogy and geochemistry (Fig. 13a), the charnockites are nearly similar to the fayalite-bearing syenites of Bachu area described by Wei and Xu (2011), except that the latter do not contain any orthopyroxene. Isotopic composition of the mafic enclave in charnockite shows an εNd value in the range of those of Tarim mafic and ultramafic dykes (Fig. 9a) with an increase in $^{87}Sr/^{86}Sr$ ratio, which is commonly linked to hydrothermal alteration (e.g., McCulloch et al., 1980). In terms of Pb isotopes, the mafic enclave is in the field of Tarim basalts and dykes (Fig. 9b). This suggests a possible common source for the magma of the mafic enclave and the Tarim mantle plume. The Pb isotopic composition of charnockites has an intermediate value between the mafic enclave and the granite resulting from

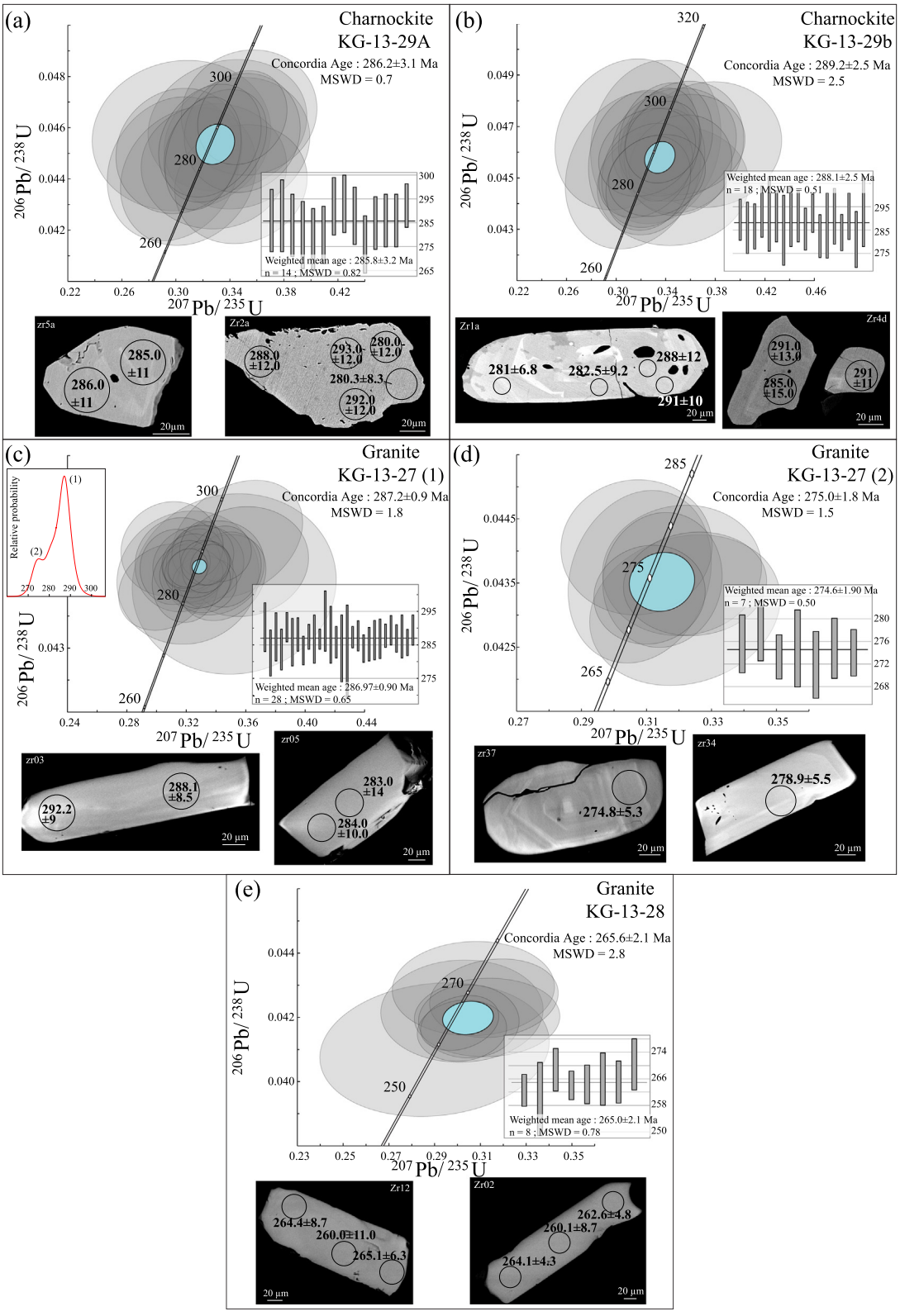

Fig. 11. Results of zircon U-Pb dating of charnockites samples KG-13-29A (a) and KG-13-29B (b) and granites resulting from partial melting of paragneisses KG-13-27 (c,d) and KG-13-28 (e). For each sample, the plot of Concordia age is shown and the weighted mean age is in the inset. Data-point error ellipse and box heights are 2σ. Representative BSE images of zircon grains for each sample are shown with the laser spot and corresponding age. In (c) the relative probability of age plot for sample KG-13-27 shows that two groups of ages can be distinguished. The first group is shown in (c) and the second group in (d).

paragneiss partial melting (Fig. 10b). We calculated a mixing line between these two end-members that suggests that charnockites result from a mixing of the mafic melt with 5 to 10 vol% of crustal melt (Fig. 9b). Thus, it is possible that charnockites isotopic composition may be influenced by some crustal contamination due to mixing with similar parganeisses. However, this hypothesis is difficult to rule out

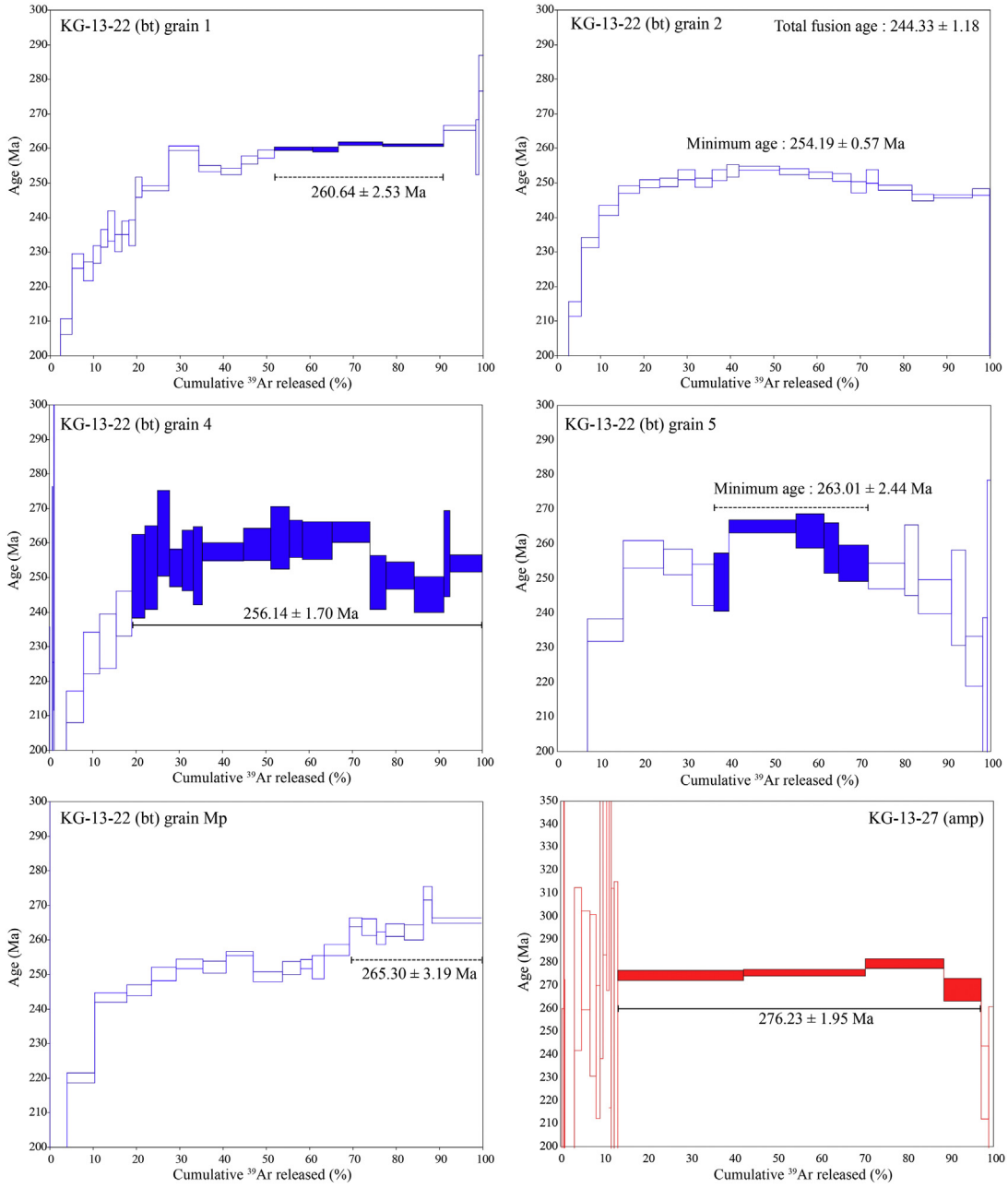

Fig. 12. $^{40}Ar/^{39}Ar$ step-heating age spectra of biotite from KG-13-22 marble and of amphibole from KG-13-27 granite. All the grains were analyzed at Geoazur (Nice) except the grain Mp, which was analyzed at Geosciences Montpellier. Dashed black line indicate "pseudo-plateau age"; i.e. plateau with <70% of ^{39}Ar released. Apparent, plateau and pseudo-plateau ages are given at 1σ.

as paragneisses are generally very variable in composition and other (lower crustal) sources might also be considered. The Hf isotopic composition of the analyzed mafic enclave is more radiogenic than that of the Tarim magmatic rocks. However, the available data regarding Hf isotopes are still scarce compared to Nd, Sr and Pb isotopes and this feature has to be confirmed. We thus propose that the charnockites result from the intrusion of a mantle-derived melt, probably linked to the Tarim mantle plume, at mid-crustal levels, where it triggered partial melting and mixing of mantle-derived (mafic enclave) and crustal (granite) melts.

9.4. Tectonic model for Pobeda charnockites emplacement

It has been suggested by many metamorphic geologists that the "continental back-arc shortening" model was the most suitable mechanism to generate HT-UHT metamorphism (e.g., Clark et al., 2011; Riel et al., 2014). However, in the Pobeda case, the subduction event had ceased in late Carboniferous and the high temperature regime was reached later on, and was certainly related to the interaction between a shortened continental (Tarim) margin and a plume-derived magma (Fig. 14; e.g., Han et al., 2016). Emplacement of granitoids in the Tien Shan range is controlled by strike-slip tectonics in numerous places (Fig. 1, e.g. Konopelko et al., 2009; B. Wang et al., 2014; F. Wang et al., 2014; Wang et al., 2009). The Pobeda charnockites outcrop on the hanging wall of a major thrust, the 'Pobeda thrust', and their syn-tectonic character, which is not apparent on the Kyrgyz side, may be confirmed on the Chinese side of the massif. The charnockites show weak post-emplacement deformation, which may be due to their stronger rheology than the surrounding rocks. Geochronological data in other areas of the Tien Shan range indicate that the Permian transition from convergent to transcurrent tectonics may have occurred slightly prior to the

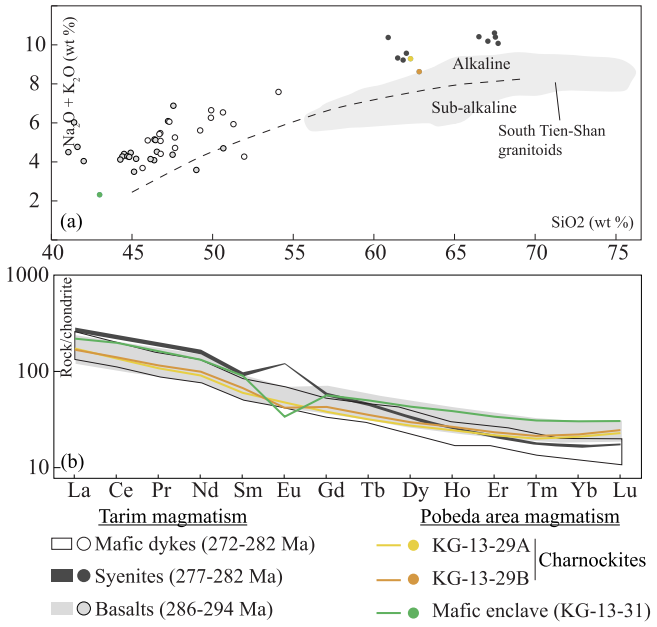

Fig. 13. Comparison of geochemistry of charnockites and mafic enclave of Pobeda area with Tarim magmatism (data after Wei and Xu, 2011; Yang et al., 2007a, 2007b; Yu et al., 2011; C.L. Zhang et al., 2010; Y. Zhang et al., 2010; Zhou et al., 2009) and South Tien Shan granitoids (data after Jiang et al., 1999; Konopelko et al., 2007, 2009). (a) SiO_2 vs. alkaline oxides diagram. The alkaline/sub-alkaline line is from Irvine and Baragar (1971). (b) Chondrite normalized rare earth elements (REE) diagram.

Pobeda magmatism, at 295–290 Ma (e.g. Konopelko et al., 2009; Laurent-Charvet et al., 2003). We thus tentatively propose that the lithosphere-scale faults of the South Tien Shan explain the ascent of mantle-derived magmas originated from the Tarim mantle plume (Fig. 14). This is also supported by similar geochemical features in charnockites and Tarim magmatic rocks (see previous section). A mantle plume origin for the charnockitic magma could also explain the high geothermal gradient needed to emplace such a hot magma (>1000 °C) at mid-crustal level.

10. Conclusion

This study brings new data on the metamorphism and magmatism of the South Tien Shan. For the first time, the Charnockite unit of the Pobeda area has been investigated in terms of petrochronology, petrology and geochemical composition, which shed some light into the tectono-magmatic evolution of STS and lateral comparisons between the Tarim and Tien Shan regions:

(1) The Charnockite unit of the Pobeda area is made of fayalite-bearing charnockites of magmatic origin, which resulted from the intrusion of a > 1000 °C melt at a pressure of around 6 kbar, corresponding to a depth of ~ 20 km.
(2) The emplacement of charnockites at a mid-crustal level led to the partial melting of the surrounding paragneisses. U-Pb datings on zircon and $^{40}Ar/^{39}Ar$ dating of amphibole show that at least three episodes of partial melting occurred, which suggests several intrusions at 287, 275 and 265 Ma.
(3) Geochemistry of charnockites and of embedded mafic enclaves indicate that they probably result from the interaction of a mantle-derived melt, of common origin with the Tarim mantle plume, and a crustal melt resulting from the partial melting of host rocks.
(4) The tectonic control of lithosphere scale strike-slips faults is proposed for the lateral magmatic flow from the Tarim mantle-plume toward the Tien Shan range, at the transition with the Tarim Craton.

The Pobeda area is thus located at the boundary between two areas and two distinct systems: (i) the Tien Shan range, where strike-slip tectonics directly controlled the emplacement of granitoids, and (ii) the Tarim where a mantle plume led to the emplacement of a large igneous province. The Tien Shan strike-slip faults could have been the locus of

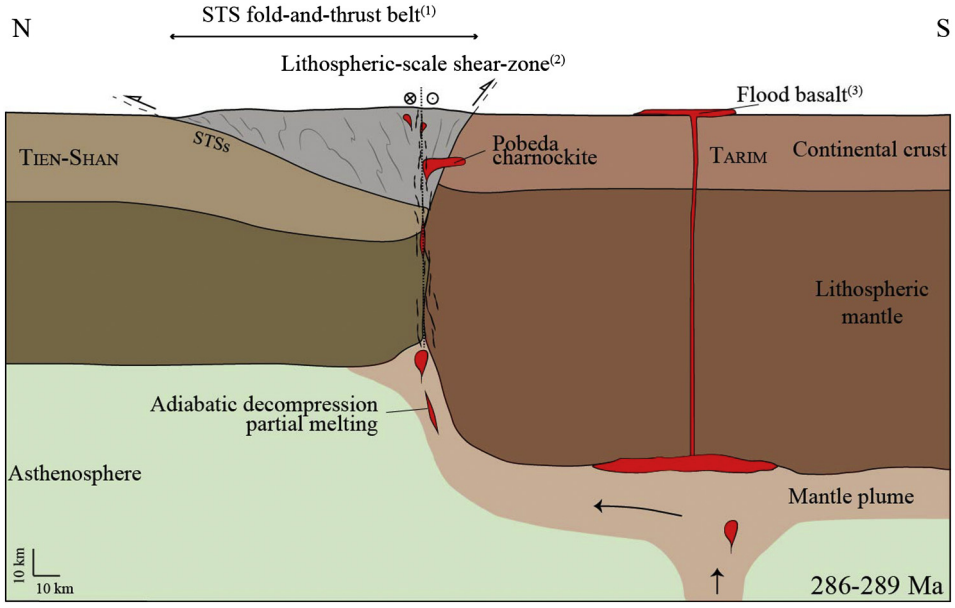

Fig. 14. Schematic diagram illustrating the proposed model for magmatism of the Pobeda area and the relations between the Tarim mantle plume and lithosphere scale strike-slip faults of the Tien Shan range. STSs: South Tien Shan suture. (1) South Tien Shan lithosphere structure is after Jourdon et al. (2017a, 2017b) and Loury et al. (2015). (2) Lithosphere scale shear zone along the South Tien Shan initiated around 295 Ma (Konopelko et al., 2009). (3) See Xu et al. (2014) for a review of the Tarim Large Igneous province.

lateral flow of the Tarim mantle plume melts rooted at the base of the lithosphere.

Acknowledgments

Field and analytical work were supported by the DARIUS Programme, coordinated by M.F. Brunet and E. Barrier and the DSP-Tibet project founded by the Agence National de la Recherche (ANR-13-BS06-012-01). We warmly thank the help of A. Mikolaichuck during field campaigns, and discussions on the Kyrgyz Tien Shan Geology. We also thank V. Magnin for assistance during microprobe analysis in Grenoble. This article benefited from fruitful comments and feedbacks from Benoît Dubacq, Qing Qian and an anonymous reviewer, which greatly improved the initial version.

Appendix A. Supplementary data

Supplementary data to this article can be found online at https://doi.org/10.1016/j.lithos.2018.01.025.

References

Ali, J.R., Thompson, G.M., Zhou, M.-F., Song, X., 2005. Emeishan large igneous province, SW China. Lithos 79:475–489. https://doi.org/10.1016/j.lithos.2004.09.013.

Avdeev, A.V., Kovalev, A.A., 1989. Ophiolites and Evolution of the Southwestern Part of the Ural–Mongolia Folded Belt (in russian).

Berger, G.W., 1975. $^{40}Ar/^{39}Ar$ step heating of thermally overprinted biotite, hornblende and potassium feldspar from Eldora, Colorado. Earth and Planetary Science Letters 26, 387–408.

Biske, Y.S., 1995. Late Paleozoic collision of the Tarimskiy and Kirghiz-Kazakh paleocontinents (English translation). Geotectonics 29, 26–34.

Biske, Y.S., Konopelko, D.L., Seltmann, R., 2013. Geodynamics of late Paleozoic magmatism in the Tien Shan and its framework. Geotectonics 47:291–309. https://doi.org/10.1134/S001685211304002X.

Bosch, D., Blichert-Toft, J., Moynier, F., Nelson, B.K., Telouk, P., Gillot, P.Y., Albarède, F., 2008. Pb, Hf and Nd isotope compositions of the two Réunion volcanoes (Indian Ocean): A tale of two small-scale mantle "blobs"? Earth and Planetary Science Letters 265:748–768. https://doi.org/10.1016/j.epsl.2007.11.018.

Bouvier, A., Vervoort, J.D., Patchett, P.J., 2008. The Lu–Hf and Sm–Nd isotopic composition of CHUR: constraints from unequilibrated chondrites and implications for the bulk composition of terrestrial planets. Earth and Planetary Science Letters 273 (1), 48–57.

Burn, M., Lanari, P., Pettke, T., Engi, M., 2017. Non-matrix-matched standardisation in LA-ICP-MS analysis: General approach, and application to allanite Th-U-Pb dating. Journal of Analytical Atomic Spectrometry https://doi.org/10.1039/C7JA00095B.

Carignan, J., Hild, P., Mevelle, G., Morel, J., Yeghicheyan, D., 2001. Routine analyses of trace elements in geological samples using flow injection and low pressure on-line liquid chromatography coupled to ICP-MS: a study of geochemical reference materials BR, DR-N, UB-N, AN-G and GH. Geostandards Newsletter 25:187–198. https://doi.org/10.1111/j.1751-908X.2001.tb00595.x.

Chapman, D.S., Pollack, H.N., 1977. Regional geotherms and lithospheric thickness. Geology 5, 265–268.

Charvet, J., Shu, L., Laurent-Charvet, S., Wang, B., Faure, M., Cluzel, D., Chen, Y., Jong, K., 2011. Palaeozoic tectonic evolution of the Tianshan belt, NW China. Science China Earth Sciences 54:166–184. https://doi.org/10.1007/s11430-010-4138-1.

Clark, C., Fitzsimons, I.C., Healy, D., Harley, S.L., 2011. How does the continental crust get really hot? Elements 7 (4), 235–240.

Connolly, J.A.D., 2009. The geodynamic equation of state: what and how. Geochemistry, Geophysics, Geosystems 10, Q10014. https://doi.org/10.1029/2009GC002540.

Frost, B.R., Frost, C.D., 2008. On charnockites. Gondwana Research 13:30–44. https://doi.org/10.1016/j.gr.2007.07.006.

Frost, B.R., Barnes, C.G., Collins, W.J., Arculus, R.J., Ellis, D.J., Frost, C.D., 2001. A geochemical classification for granitic rocks. Journal of Petrology 42:2033–2048. https://doi.org/10.1093/petrology/42.11.2033.

Fuhrman, M.L., Lindsley, D.H., 1988. Ternary-feldspar modeling and thermometry. American Mineralogist 73, 201–215.

Gao, J., Long, L., Klemd, R., Qian, Q., Liu, D., Xiong, X., et al., 2009. Tectonic evolution of the South Tianshan orogen and adjacent regions, NW China: geochemical and age constraints of granitoid rocks. International Journal of Earth Sciences 98 (6), 1221.

Gao, J., Klemd, R., Qian, Q., Zhang, X., Li, J., Jiang, T., Yang, Y., 2011. The collision between the Yili and Tarim blocks of the Southwestern Altaids: geochemical and age constraints of a leucogranite dike crosscutting the HP–LT metamorphic belt in the Chinese Tianshan Orogen. Tectonophysics 499 (1), 118–131.

Grove, M., Harrison, T.M., 1996. $^{40}Ar^*$ diffusion in Fe-rich biotite. American Mineralogist 81, 940–951.

Han, Y., Zhao, G., Sun, M., Eizenhöfer, P.R., Hou, W., Zhang, X., et al., 2016. Late Paleozoic subduction and collision processes during the amalgamation of the Central Asian Orogenic Belt along the South Tianshan suture zone. Lithos 246, 1–12.

Harrison, T.M., 1982. Diffusion of ^{40}Ar in hornblende. Contributions to Mineralogy and Petrology 78, 324–331.

Hegner, E., Klemd, R., Kröner, A., Corsini, M., Alexeiev, D.V., Iaccheri, L.M., Zack, T., Dulski, P., Xia, X., Windley, B.F., 2010. Mineral ages and P-T conditions of Late Paleozoic high-pressure eclogite and provenance of melange sediments from Atbashi in the south Tianshan orogen of Kyrgyzstan. American Journal of Science 310:916–950. https://doi.org/10.2475/09.2010.07.

Holland, T.J.B., Blundy, J., 1994. Non-ideal interactions in calcic amphiboles and their bearing on amphibole-plagioclase thermometry. Contributions to Mineralogy and Petrology 116:433–447. https://doi.org/10.1007/BF00310910.

Holland, T., Powell, R., 1996. Thermodynamics of order-disorder in minerals: I. Symmetric formalism applied to minerals of fixed composition. American Mineralogist 81, 1413–1424.

Holland, T.J.B., Powell, R., 1998. An internally consistent thermodynamic data set for phases of petrological interest. Journal of Metamorphic Geology 16, 309–343.

Huppert, H.E., Sparks, R.S.J., 1988. The generation of granitic magmas by intrusion of basalt into continental crust. Journal of Petrology 29:599–624. https://doi.org/10.1093/petrology/29.3.599.

Irvine, T.N., Baragar, W.R.A., 1971. A guide to the chemical classification of the common volcanic rocks. Canadian Journal of Earth Sciences 8, 523–548.

Jackson, S.E., Pearson, N.J., Griffin, W.L., Belousova, E.a., 2004. The application of laser ablation-inductively coupled plasma-mass spectrometry to in situ U-Pb zircon geochronology. Chemical Geology 211:47–69. https://doi.org/10.1016/j.chemgeo.2004.06.017.

Jiang, C., Mu, Y., Bai, K., Zhao, X., Zhang, H., Hei, A., 1999. Chronology, petrology, geochemistry and tectonic environment of granitoids in the southern Tianshan Mountain, western China (in chinese with english abstract). Acta Petrologica Sinica 15, 298–308.

de Jong, K., Wang, B.B., Faure, M., Shu, L., Cluzel, D., Charvet, J., Ruffet, G., Chen, Y., 2009. New $^{40}Ar/^{39}Ar$ age constraints on the Late Palaeozoic tectonic evolution of the western Tianshan (Xinjiang, northwestern China), with emphasis on Permian fluid ingress. International Journal of Earth Sciences 98:1239–1258. https://doi.org/10.1007/s00531-008-0338-8.

Jourdan, F., Renne, P.R., 2007. Age calibration of the Fish Canyon sanidine $^{40}Ar/^{39}Ar$ dating standard using primary K-Ar standards. Geochimica et Cosmochimica Acta 71, 387–402.

Jourdon, A., Petit, C., Rolland, Y., Loury, C., Bellahsen, N., Guillot, S., Le Pourhiet, L., Ganino, C., 2017a. New structural data on Late Paleozoic tectonics in the Kyrgyz Tien Shan (Central Asian Orogenic Belt). Gondwana Research 46:57–78. https://doi.org/10.1016/j.gr.2017.03.004.

Jourdon, A., Le Pourhiet, L., Petit, C., Rolland, Y., 2017b. The deep structure and reactivation of the Kyrgyz Tien Shan: modelling the past to better constrain the present. Tectonophysics https://doi.org/10.1016/j.tecto.2017.07.019.

Jourdon, A., Le Pourhiet, L., Petit, C., Rolland, Y., 2018. Impact of range-parallel sediment transport on mountain building and exhumation in Kyrgyz Tien Shan. Terra Nova (accepted for publication).

Konopelko, D., Biske, G., Seltmann, R., Eklund, O., Belyatsky, B., 2007. Hercynian post-collisional A-type granites of the Kokshaal Range, Southern Tien Shan, Kyrgyzstan. Lithos 97:140–160. https://doi.org/10.1016/j.lithos.2006.12.005.

Konopelko, D., Seltmann, R., Biske, G., Lepekhina, E., Sergeev, S., 2009. Possible source dichotomy of contemporaneous post-collisional barren I-type versus tin-bearing A-type granites, lying on opposite sides of the South Tien Shan suture. Ore Geology Reviews 35:206–216. https://doi.org/10.1016/j.oregeorev.2009.01.002.

Konopelko, D., Seltmann, R., Apayarov, F., Belousova, E., Izokh, A., Lepekhina, E., 2013. U–Pb–Hf zircon study of two mylonitic granite complexes in the Talas-Fergana fault zone, Kyrgyzstan, and Ar–Ar age of deformations along the fault. Journal of Asian Earth Sciences 73:334–346. https://doi.org/10.1016/j.jseaes.2013.04.046.

Kröner, A., Alexeiev, D.V., Rojas-Agramonte, Y., Hegner, E., Wong, J., Xia, X., Belousova, E., Mikolaichuk, A.V., Seltmann, R., Liu, D., Kiselev, V.V., 2013. Mesoproterozoic (Grenville-age) terranes in the Kyrgyz North Tianshan: Zircon ages and Nd-Hf isotopic constraints on the origin and evolution of basement blocks in the southern Central Asian Orogen. Gondwana Research 23:272–295. https://doi.org/10.1016/j.gr.2012.05.004.

Kunz, B.E., Manzotti, P., von Niederhäusern, B., Engi, M., Darling, J.R., Giuntoli, F., Lanari, P., 2017. Permian high-temperature metamorphism in the Western Alps (NW Italy). International Journal of Earth Sciences:1–27 https://doi.org/10.1007/s00531-017-1485-6.

Laurent-Charvet, S., Charvet, J., Monié, P., Shu, L., 2003. Late Paleozoic strike-slip shear zones in eastern central Asia (NW China): new structural and geochronological data. Tectonics 22:1009. https://doi.org/10.1029/2001TC901047.

Le Bas, M.J., Streckeisen, A.L., 1991. The IUGS systematics of igneous rocks. Journal of the Geological Society of London 148, 825–833.

Leake, B.E., 1978. Nomenclature of amphiboles. American Mineralogist 63, 1023–1052.

Li, Q., Lin, W., Su, W., Li, X., Shi, Y., Liu, Y., Tang, G., 2011. SIMS U–Pb rutile age of low-temperature eclogites from southwestern Chinese Tianshan, NW China. Lithos 122: 76–86. https://doi.org/10.1016/j.lithos.2010.11.007.

Li, Z., Li, Y., Chen, H., Santosh, M., Yang, S., Xu, Y., Langmuir, C.H., Chen, Z., Yu, X., Zou, S., 2012. Hf isotopic characteristics of the Tarim Permian large igneous province rocks of NW China: implication for the magmatic source and evolution. Journal of Asian Earth Sciences 49:191–202. https://doi.org/10.1016/j.jseaes.2011.11.021.

Loury, C., Rolland, Y., Guillot, S., Mikolaichuk, A.V., Lanari, P., Bruguier, O., Bosch, D., 2015. Crustal-scale structure of South Tien Shan: implications for subduction polarity and Cenozoic reactivation. In: Brunet, M.F., McCann, T., Sobel, E.R. (Eds.), Geological Evolution of Central Asian Basins and the Western Tien-Shan Range. The Geological Society of London https://doi.org/10.1144/SP427.4.

Loury, C., Rolland, Y., Cenki-Tok, B., Lanari, P., Guillot, S., 2016. Late Paleozoic evolution of the South Tien Shan: Insights from P-T estimates and allanite geochronology on retrogressed eclogites (Chatkal range, Kyrgyzstan). Journal of Geodynamics 96: 62–80. https://doi.org/10.1016/j.jog.2015.06.005.

Ludwig, K.R., 2003. Isoplot 3.00 a Geochronological Toolkit for Microsoft Excel. Berkley Geochronol. Cent. Spec. Pub. 4.
Makarov, V.I., Alekseev, D.V., Batalev, V.Y., Bataleva, E.A., Belyaev, I.V., Bragin, V.D., Dergunov, N.T., Efimova, N.N., Leonov, M.G., Munirova, L.M., Pavlenkin, A.D., Roecker, S., Roslov, Y.V., Rybin, A.K., Shchelochkov, G.G., 2010. Underthrusting of Tarim beneath the Tien Shan and deep structure of their junction zone: main results of seismic experiment along MANAS Profile Kashgar-Song-Köl. Geotectonics 44: 102–126. https://doi.org/10.1134/S0016852110020020.
McCulloch, M.T., Gregory, R.T., Wasserburg, G.J., Taylor, H.P., 1980. A neodymium, strontium, and oxygen isotopic study of the Cretaceous Samail Ophiolite and implications for the petrogenesis and seawater-hydrothermal alteration of oceanic crust. Earth and Planetary Science Letters 46, 201–211.
Mikolaichuk, A.V., Buchroithner, M., 2008. Quaternary Removed Geological Map of the Khan Tengri Massif (ISTC Project {#}KR-920)(1:200000). Kyrg. Slav. Univ. Int. Sci. Technol. Cent.
Mikolaichuk, A.V., Kurenkov, S.A., Degtyarev, K.E., Rubstov, V.I., 1997. Northern Tianshan, main stages of geodynamic evolution in the late Precambrien and early Paleozoic. Geotectonics 31, 445–462.
Morimoto, N., 1988. Nomenclature of pyroxenes. American Mineralogist 73, 1123–1133.
Paton, C., Hellstrom, J., Paul, B., Woodhead, J., Hergt, J., 2011. Iolite: freeware for the visualisation and processing of mass spectrometric data. Journal of Analytical Atomic Spectrometry 26, 2508–2518.
Pearce, J.A., 1996. A user's guide to basalt discrimination diagrams. In: Wyman, D.A. (Ed.), Trace Element Geochemistry of Volcanic Rocks: Applications for Massive Sulphide Exploration. Geological Association of Canada, pp. 79–113 (Short Course Notes).
Petrus, J.A., Kamber, B.S., 2012. VizualAge: a novel approach to laser ablation ICP-MS U-Pb geochronology data reduction. Geostandards and Geoanalytical Research 36, 247–270.
Pirajno, F., 2010. Intracontinental strike-slip faults, associated magmatism, mineral systems and mantle dynamics: Examples from NW China and Altay-Sayan (Siberia). Journal of Geodynamics 50:325–346. https://doi.org/10.1016/j.jog.2010.01.018.
Renne, P., Basu, A.R., 1991. Rapid eruption of the Siberian traps flood basalts at the Permo-Triassic boundary. Science 253, 176–179 (80-.).
Riel, N., Martelat, J.E., Guillot, S., Jaillard, E., Monié, P., Yuquilema, Y., Duclaux, G., Mercier, J., 2014. Fore arc tectonothermal evolution of the El Oro metamorphic province (Ecuador) during the Mesozoic. Tectonics 33. https://doi.org/10.1002/2014TC003618.
Rolland, Y., Alexeiev, D.V., Kröner, A., Corsini, M., Loury, C., Monié, P., 2013. Late Palaeozoic to Mesozoic kinematic history of the Talas-Ferghana strike-slip fault (Kyrgyz West Tianshan) as revealed by 40Ar/39Ar dating of syn-kinematic white mica. Journal of Asian Earth Sciences 67–68:76–92. https://doi.org/10.1016/j.jseaes.2013.02.012.
Rubatto, D., 2002. Zircon trace element geochemistry: partitioning with garnet and the link between U–Pb ages and metamorphism. Chemical Geology 184:123–138. https://doi.org/10.1016/S0009-2541(01)00355-2.
Schmidt, M.W., 1992. Amphibole composition in tonalite as a function of pressure: an experimental calibration of the Al-in-hornblende barometer. Contributions to Mineralogy and Petrology 110:304–310. https://doi.org/10.1007/BF00310745.
Shu, L., Charvet, J., Lingzhi, G., Lu, H., Laurent-charvet, S., 1999. A large-scale Palaeozoic dextral ductile strike-slip zone: the Aqqikkudug-Weiya zone along the northern margin of the central Tianshan Belt, Xinjiang, NW China. Acta Geologica Sinica 73, 148–162.
Sláma, J., Košler, J., Condon, D.J., Crowley, J.L., Gerdes, A., Hanchar, J.M., Horstwood, M.S.A., Morris, G.A., Nasdala, L., Norberg, N., Schaltegger, U., Schoene, B., Tubrett, M.N., Whitehouse, M.J., 2008. Plešovice zircon - a new natural reference material for U-Pb and Hf isotopic microanalysis. Chemical Geology 249, 1–35.
Steiger, R.H., Jäger, E., 1977. Subcommission on geochronology: convention on the use of decay constants in geo- and cosmochronology. Earth and Planetary Science Letters 36, 359–362.
Streckeisen, A., 1974. Classification and nomenclature of plutonic rocks recommendations of the IUGS subcommission on the systematics of igneous rocks. Geologische Rundschau 63, 773–786.
Sun, S.S., McDonough, W.F., 1989. Chemical and isotopic systematics of oceanic basalts: implications for mantle composition and processes. Geological Society of London, Special Publication 42:313–345. https://doi.org/10.1144/GSL.SP.1989.042.01.19.
Thompson, A.B., 1982. Dehydration melting of pelitic rocks ans the generation of H_2O undersaturated granitic liquids. American Journal of Science 282, 1567–1595.
Tian, W., Campbell, I.H., Allen, C.M., Guan, P., Pan, W., Chen, M., et al., 2010. The Tarim picrite–basalt–rhyolite suite, a Permian flood basalt from northwest China with contrasting rhyolites produced by fractional crystallization and anatexis. Contributions to Mineralogy and Petrology 160 (3), 407–425.
Touret, J.L.R., Huizenga, J.M., 2012. Charnockite microstructures: from magmatic to metamorphic. Geoscience Frontiers 3:745–753. https://doi.org/10.1016/j.gsf.2012.05.004.
Turner, F.J., 1981. Metamorphic Petrology: Mineralogical, Field, and Tectonic Aspects. McGraw-Hill Companies.
Tursungaziev, B.T., Petrov, O.V., 2008. Geological Map of Kirghyz Republic, Scale 1:500000. (in russian). VSEGEI, Saint-petersbg.
Wang, B., Chen, Y., Zhan, S., Shu, L., Faure, M., Cluzel, D., Charvet, J., Laurent-charvet, S., 2007a. Primary carboniferous and Permian paleomagnetic results from the Yili Block (NW China) and their implications on the geodynamic evolution of Chinese Tianshan Belt. Earth Planet. Science Letters 263:288–308. https://doi.org/10.1016/j.epsl.2007.08.037.
Wang, H.L., Xu, X.Y., He, S.P., Chen, J.L., 2007b. China Geological Map of the Tianshan and Adjacent Areas: 1:1000000. Chinese edition. Geological Publishing House, China.
Wang, B., Cluzel, D., Shu, L., Faure, M., Charvet, J., Chen, Y., Meffre, S., Jong, K., 2009. Evolution of calc-alkaline to alkaline magmatism through Carboniferous convergence to Permian transcurrent tectonics, western Chinese Tianshan. International Journal of Earth Sciences 98:1275–1298. https://doi.org/10.1007/s00531-008-0408-y.
Wang, B., Cluzel, D., Jahn, B., Shu, L., Chen, Y., Zhai, Y., Branquet, Y., Barbanson, L., Sizaret, S., 2014a. Late Paleozoic pre- and syn-kinematic plutons of the Kangguer–Huangshan Shear zone: inference on the tectonic evolution of the eastern Chinese north Tianshan. American Journal of Science 314:43–79. https://doi.org/10.2475/01.2014.02.
Wang, F., Zhu, R., Hou, Q., Zheng, D., Yang, L., Wu, L., Shi, W., Feng, H., Sang, H., Zhang, H., Liu, Q., 2014b. $^{40}Ar/^{39}Ar$ thermochronology on Central China Orogen: cooling, uplift and implications for orogeny dynamics. In: Jourdan, F., Mark, D.F., Verati, C. (Eds.), Advances in $^{40}Ar/^{39}Ar$ Dating: From Archaeology to Planetary Sciences. Geological Society, London, Special Publications:pp. 189–206 https://doi.org/10.1144/SP378.3.
Wei, X., Xu, Y., 2011. Petrogenesis of the Xiaohaizi syenite complex from the Bachu area, Tarim (in chinese with english abstract). Acta Petrologica Sinica 27, 2984–3004.
Wei, X., Xu, Y., Feng, Y., Zhao, J., 2014. Plume-lithosphere interactions in the generation of the Tarim large igneous province, NW China: geochronological and geochemical constraints. American Journal of Science 314:314–356. https://doi.org/10.2475/01.2014.09.
White, W.M., 2013. Geochemistry. Wiley-Blac. ed.
White, R.W., Powell, R., Holland, T.J.B., 2001. Calculation of partial melting equilibria in the system Na_2O-CaO-K_2O-FeO-MgO-Al_2O_3-SiO_2-H_2O (NCKFMASH). Journal of Metamorphic Geology 19, 139–153.
Windley, B.F., Allen, M.B., Zhang, C., Zhao, Z.-Y., Wang, G.-R., 1990. Paleozoic accretion and Cenozoic redeformation of the Chinese Tien Shan Range, central Asia. Geology 18: 128. https://doi.org/10.1130/0091-7613(1990)018<0128:PAACRO>2.3.CO;2.
Xu, Y.G., Wei, X., Luo, Z.Y., Liu, H.Q., Cao, J., 2014. The Early Permian Tarim large igneous province: main characteristics and a plume incubation model. Lithos 204:20–35. https://doi.org/10.1016/j.lithos.2014.02.015.
Yang, S.F., Li, Z., Chen, H., Santosh, M., Dong, C.W., Yu, X., 2007a. Permian bimodal dyke of Tarim Basin, NW China: geochemical characteristics and tectonic implications. Gondwana Research 12:113–120. https://doi.org/10.1016/j.gr.2006.10.018.
Yang, S.F., Li, Z.L., Chen, H.L., Santosh, M., Yu, X., 2007b. Discovery of Permian bimodal dyke: geochemistry and implications for tectonic evolution related to the last major tectono-thermal event in Tarim Basin, NW China. Gondwana Research 12, 113–120.
Yang, S.F., Chen, H., Li, Z., Li, Y., Yu, X., Li, D., Meng, L., 2013. Early Permian Tarim large igneous province in northwest China. Science China Earth Sciences 56:2015–2026. https://doi.org/10.1007/s11430-013-4653-y.
Yu, X., Yang, S.-F., Chen, H.-L., Chen, Z.-Q., Li, Z.-L., Batt, G.E., Li, Y.-Q., 2011. Permian flood basalts from the Tarim Basin, Northwest China: SHRIMP zircon U–Pb dating and geochemical characteristics. Gondwana Research 20:485–497. https://doi.org/10.1016/j.gr.2010.11.009.
Zhang, C.-L., Zou, H.-B., 2013. Permian A-type granites in Tarim and western part of Central Asian Orogenic Belt (CAOB): genetically related to a common Permian mantle plume? Lithos 172–173:47–60. https://doi.org/10.1016/j.lithos.2013.04.001.
Zhang, C.L., Li, Z.X., Li, X.H., Xu, Y.G., Zhou, G., Ye, H.M., 2010a. A Permian large igneous province in Tarim and Central Asian orogenic belt, NW China: Results of a ca. 275 Ma mantle plume? Bulletin Geological Society of America 122:2020–2040. https://doi.org/10.1130/B30007.1.
Zhang, Y., Liu, J., Guo, Z., 2010b. Permian basaltic rocks in the Tarim basin, NW China: implications for plume–lithosphere interaction. Gondwana Research 18:596–610. https://doi.org/10.1016/j.gr.2010.03.006.
Zhang, D., Zhou, T., Yuan, F., Jowitt, S.M., Fan, Y., Liu, S., 2012. Source, evolution and emplacement of Permian Tarim Basalts: evidence from U-Pb dating, Sr-Nd-Pb-Hf isotope systematics and whole rock geochemistry of basalts from the Keping area, Xinjiang Uygur Autonomous region, northwest China. Journal of Asian Earth Sciences 49: 175–190. https://doi.org/10.1016/j.jseaes.2011.10.018.
Zhou, M.-F., Zhao, J.-H., Jiang, C.-Y., Gao, J.-F., Wang, W., Yang, S.-H., 2009. OIB-like, heterogeneous mantle sources of Permian basaltic magmatism in the western Tarim Basin, NW China: implications for a possible Permian large igneous province. Lithos 113: 583–594. https://doi.org/10.1016/j.lithos.2009.06.027.